# Synthesis of Trimetallic ($SiO_2$@AuPtPd) Core Shell Nanoparticles and its Structural Characterization

Krishna Daware, Gaurav Lole, and Suresh Gosavi*
Centre for Advanced Studies in Material Science and Solid State Physics,
Department of Physics, Savitribai Phule Pune University, (Formerly University of Pune) Ganeshkhind,
Pune - 411007, INDIA
Author to whom correspondence should be address Email: swg@physics.unipune.ac.in

## Abstract:

**We have successfully synthesized Silica@Gold-Platinum-Palladium ($SiO_2$@AuPtPd) timetalic core shell nanoparticles using chemical method. The synthesized nanoparticles are characterized using field emission scanning electron microscopy (FESEM) and Transmission electron microscopy (TEM). The FESEM micrograph shows the monodispersed silica nanoparticles having spherical shape, decorated with quantum dot of Au, Pt and Pd metal nanoparticles. The average particle size of $SiO_2$ nanoparticles is ~150nm where as Au, Pt and Pd metal nanoparticles are ~8nm in size. The energy dispersive spectra of $SiO_2$@AuPtPd nanoparticles also shows the presence of O, Si, Pd, Pt and Au nanoparticles with atomic percentage of 75.48, 23.08, 1.05, 0.21 and 0.17% respectively. The elemental mapping also confirms the decoration of Pt, Pd and Au nanoparticles on the large surface of $SiO_2$ nanoparticles.**

**Introduction:** Colloidal core-shell nanoparticles are paying attention towards significant importance due to their definite nanostructure, composition and particle size. Trimetallic core-shell nanoparticles shows enhancement in their magnetic, optical, electrical and catalytic properties. Au-, Pd-, and Pt-based core-shell nanoparticles have shown outstanding optical and catalytic properties which are not achievable by their monometallic composition. Furthermore, the mentioned core-shell trimetallic nanoparticles are frequently synthesized by a chemical method. Therefore, core-shell nanoparticles with multiple compositions is an imposing challenge for the growth of elegant nanostructured materials. For instance, multi composition core-shell structured nano architectures consisting of Au, Pd and Pt are expected to be promising materials in catalysis, hydrogen storage and surface enhanced Raman scattering (SERS) studies. Due to interesting physicochemical properties resulting from the combination of three types of metals and their fine structures, the combination of gold, platinum and palladium is one of the most popular examples. In the present work we report $SiO_2$@AuPtPd trimetalic core shell nanostructure using simple chemical route method[1,3].

**Experimental:** Tetraethylorthosilicate (TEOS), Chloroauric acid ($HAuCl_4$), Chloroplatinic acid ($H_2PtCl_6$), ($H_2PdCl_4$), sodium borohydride ($NaBH_4$), Absolute Ethanol were purchased from Sigma-Aldrich. Ammonia (about 25% in water) were purchased from Thomas Baker. The synthesized particles were separated from reaction vessel/aqueous medium by centrifugation (Model: Minispin eppendorf) method. All the glassware's were cleaned by freshly prepared aqua-regia ($HCl:HNO_3$) solution and rinsed with distilled water before experiment. All the stock solutions were prepared in de-ionized water.

Silica core nanoparticles are synthesized by Stober method which involves the hydrolysis and condensation of TEOS by a sol–gel process. The schematic representation of the process is shown in the following fig.1

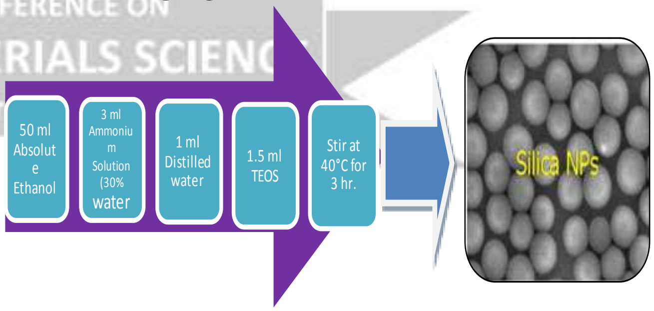

*Fig.1. Schematic representation of synthesis of silica nanoparticles by using Stober method*

In a typical procedure, 1.5 ml of Tetraethyl orthosilicate (TEOS) was added into the mixture of 50 ml absolute ethanol, 3 ml $NH_3$ (about 30% in water) and 1 ml distilled water. The solution is continually stirred for 3 hrs at 40 °C. After 3 hrs of reaction, an additional 1ml of TEOS was added, which was followed by stirring for another 3 hrs of reaction at 40°C. With the help of centrifugation (1300rpm for 10min), silica nanoparticles were separated and washed with absolute ethanol.

The $SiO_2$@AuPtPd nanoparticles were synthesized by simple mixing of Au, Pt, and Pd into the silica particle's solution. The 50 mL above prepared silica particles solution and 50 mL of mixture of gold platinum and palladium nanoparticle solution was mixed under stirring for 24 hrs at 45°C. The color of the resultant solution turned into grey which indicates the formation of decorated $SiO_2$@AuPtPd nanoparticles. The Au, Pt and Pd nanoparticles are decorated on the top surface of the spherical silica nanoparticles. The decoration of Au, Pt and Pd nanoparticles on silica particles was confirmed by physical techniques such as FE-SEM, EDX, TEM and elemental mapping using TEM[4, 5].

**Results and conclusion:** The formation of $SiO_2$@AuPtPd core shell nanoparticles was conformed using FESEM spectroscopy. FESEM measurements were carried out on Nova NanoSEM 450 instrument operated at an accelerating voltage at 30 KV. Sample was prepared by drop casting on silicon substrate and coating by gold. The FESEM micrographs (Fig.2) show the spherical and monodispersed silica nanoparticles decorated with gold, platinum and palladium nanoparticles.

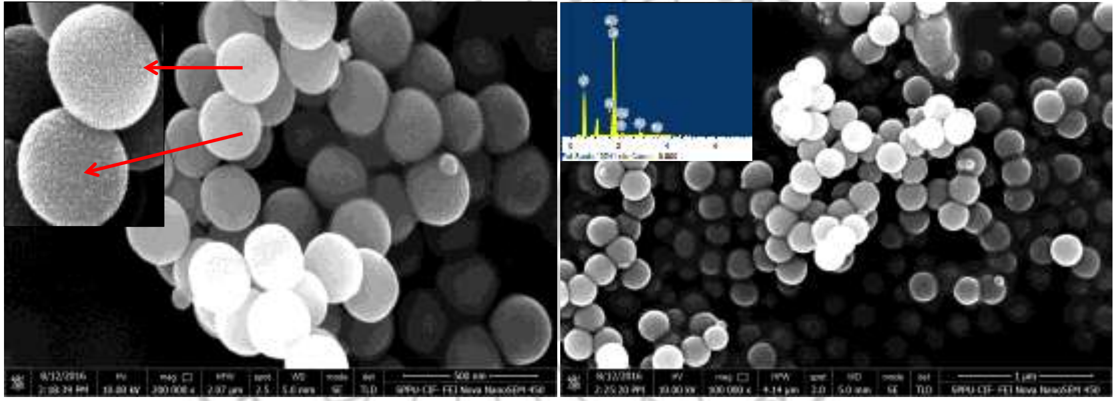

***Fig. 2** FESEM micrographs of $SiO_2$@AuPtPd trimetallic nanoparticles*

The energy dispersive spectra of synthesized $SiO_2$@AuPtPd core shell nanoparticles also confirms the presence of pure silica and gold, platinum, palladium as shown in inset. The measured atomic percentage of oxygen, silicon, palladium, platinum, and gold are 75.48, 23.08, 1.05, 0.21 and 0.17% % respectively[6, 7].

The synthesized $SiO_2$@AuPtPd core shell nanoparticles were also confirmed using TEM microscopy and elemental mapping by TEM. TEM measurements were performed on a TECNAI G$^2$ 20 instrument operated at an accelerating voltage at 200KV. Sample for TEM was prepared by drop casting of sample on carbon coated copper grid. The fig. 3 shows TEM micrographs of $SiO_2$@AuPtPd core shell nanoparticles which also confirm the formation of $SiO_2$@AuPtPd core shell nanoparticles.

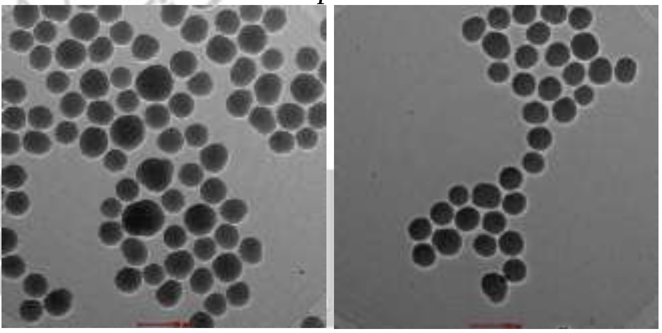

***Fig. 3** TEM micrograph of $SiO_2$@AuPtPd trimetallic nanoparticles*

The elemental mapping of $SiO_2$@AuPtPd core shell nanoparticles was studied by EDX (Model: Bruker equipped with TEM instrument which also confirms formation SiO2@AuPtPdcore-shell nanoparticles.

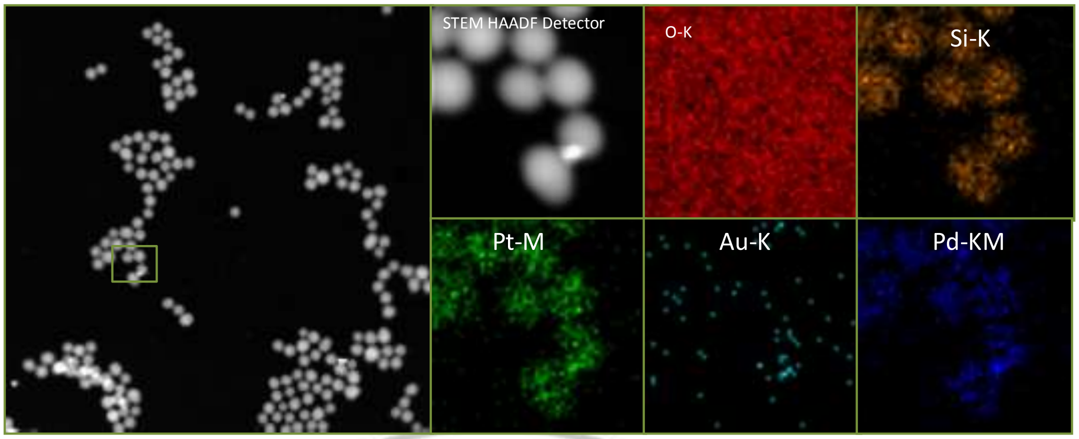

*Fig. 4 Elemental mapping using TEM instrument*

## Conclusion:

**The development of simple route for the synthesis of silica@metal core-shell nanoparticles by chemical method is successfully reported here. The synthesized nanostructures have silica as a core ~150nm and gold, platinum, palladium ~ 8nm as shell. $SiO_2$@AuPtPd core shell nanoparticles are extensively used for various biological applications ranging from bio-analysis and bio-imaging to diagnosis and therapy. It is also important in catalysis, hydrogen storage, and surface enhanced Raman scattering (SERS) studies.**

## References

[1] Liang Wang, et.al. Jacs Communication, (2010)10.1021
[2] Yoshiteru Mizukoshi, et.al. J. Physics Chem, (2000) 10.1021
[3] N.R. Jana et. al. Langmuir. 16 (2000) 2457.
[4] K. Mallick at.al. Mater. Chem. Phys. 97 (2006) 283.
[5] M.N. Nadagouda et.al. RSC Adv. 2 (2012) 7540
[6] N. Cheval at.al. Nanoscale Res. Lett. 7 (2012) 182.
[7] N.R. Jana et.al. J. Phys. Chem. B. 103 (1999) 115–121.

# Synthesis, Characterization and Photocatalytic activity of $Fe_2O_3$

A M. Sargar*, P.S. Dikule
P. G. Department of Chemistry, Bharati Vidyapeeth's, Dr. Patengrao Kadam Mahavidyalaya, Sangli, (MS) India.Email: ankush_chem@rediffmail.com

## Abstract

**Our aim to synthesize $Fe_2O_3$ by innovative synthesis route i.e. auto-combustion technique. Thermal stability of prepared oxide was carried out using TG-DTA analysis, which indicates prepared oxide was stable at 700°C. Phase formation of oxide material was carried out by FTIR study. Photocatalytic activity of prepared $Fe_2O_3$ material carried out by using malachite green dye.**

**Keywords: Photocatalytic activity, TG-DTA, Malachite green.**

## 1. Introduction:

In recent years, the use of semiconductor metal oxides as photocatalysts for degradation of pollutants has attracted attention of scientific community. Semiconductor metal oxide nanoparticles have been studied due to their novell optical, electronic, magnetic, thermal and mechanical properties and potential application in catalyst, gas-sensors and photo-electronic devices [1-5]. The most common semiconducting metal oxides are $TiO_2$ and ZnO due to their catalytic. The photocatalytic process starts with the irradiation of a semiconductor material by light with sufficient energy to excite the electrons from the valence band to the conduction band generating extremely reactive electron/hole (e-/h+) pairs that migrate to the adsorbed species leading to reactive species such as hydroxyl radicals. The major drawback of the photocatalytic process is the electron/hole pair recombination. To solve this problem metal oxide nanoparticles are embedded into different matrices.

The photocatalytic activity of semiconducting metal oxide can be effectively modified by ionizing radiations. These radiations induce some changes in the structural, textural, electric, magnetic and catalytic properties of the treated solids. For instance gamma-rays have been reported to effect some changes in the chemistry of surfaces of the semiconducting metal oxides [6-10]. In the present work, auto-combustion method was chosen for the synthesis of nanostructured $Fe_2O_3$. The obtained products characterized by different physicochemical techniques such as TG-DTA and FTIR. The obtained product has more excellent photocatalytic activity under UV light for the degradation of malachite green.

## 2. Experimental

$Fe_2O_3$ was synthesized by auto-combustion method. The synthesis was carried out with the $Fe(NO_3)_2{\cdot}9H_2O$ as the Fe source, and glycine used as fuel. The raw materials used in the experiment were all of analytical purity. Firstly, stoichiometric amount $Fe(NO_3)_2{\cdot}9H_2O$ was dissolved in doubly distilled water with vigorous stirring. Glycine was weighted stoichiometrically and dissolved in distilled water. The ratio of nitrate to fuel is 1:2. The above solution mixed under stirring and pH adjusted to 9.5 using ammonia solution. A homogeneous clear solution was achieved. This content was stirred and heated at 800°C for 2 hr to obtain gel. This gel was heated on hot plate at 300-400°C to obtain oxide powder. This powder was calcined at 450-700°C for 3 hr. Synthesis route is shown in flowchart.

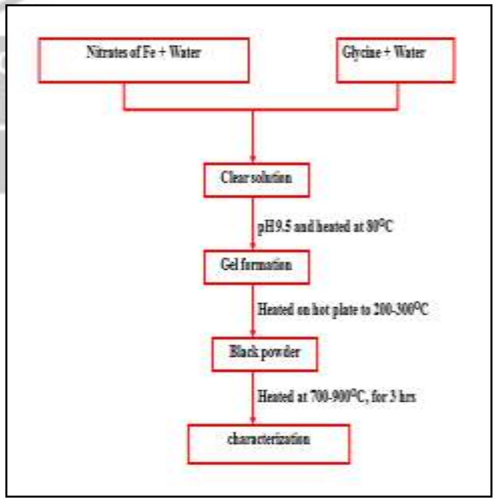

The TGA-DTA measurements were carried out using instrument Model SDT Q-600 under dried air atmosphere from room temperature to $1000^0$C at a heating rate of $10^0$C/min. JASCO FT/IR-6100 type ‘A’ spectrometer was used for FTIR study. UV-Visible spectral measurements were made using Systronic AU-2700 double beam UV/Visible spectrophotometer. The pH of the solution was measured by HANNA phep (model H 19) digital pH meter.

### 2.1 Photodegradation of malachite green (MG):

Ultra-violet light photocatalytic activities of the obtained photocatalyst were measured by the decomposition of malachite green in an aqueous solution at ambient temperature. A cut-off filter was placed under the UV lamp (230 V) to remove all wave lengths less than 400 nm. In each experiment, 0.2 g of photocatalyst was added into 50 ml malachite green solution with a concentration of 10 ppm. The suspension was magnetically stirred in the dark for 30 min to establish the adsorption/desorption equilibrium at room temperature, then the solution was irradiated using UV radiation. During irradiation, stirring was maintained to keep the mixture in suspension. At regular intervals, samples were taken from the suspension and then centrifuged to remove the photocatalyst particles. The change in the concentration of each degraded solution was monitored on UV-Visible spectral measurements were made using Systronic AU-2700 double beam UV/Visible spectrophotometer for malachite green. Distilled water was used as the reference sample.

## 3. Results and discussion:

### 3.1 TGA-DTA Analysis:

TGA-DTA analysis of $Fe_2O_3$ sample heated at the rate $10^0$C/minute from 0 to $1000^0$C, is given in figures 1. The TGA curve shows thermal decomposition of $Fe_2O_3$ below $200^0$C due to removal of absorbed water and at $350^0$C is ascribed due to thermal decomposition of organic residue. The dehydration also produces TGA weight loss in the region of 100–200°C and this loss is due to auto catalytic oxidation reduction reactions of nitrates with citric acid.

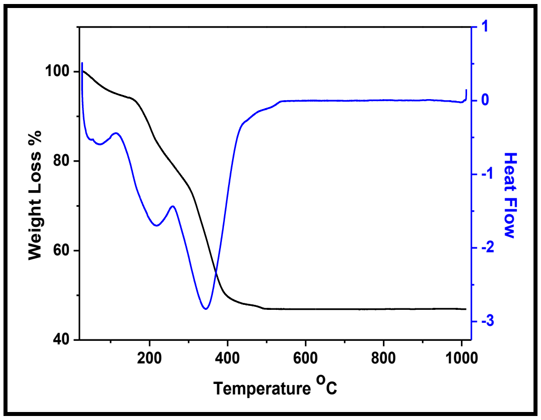

**Fig. 1.** TGA-DTA curve of as synthesized $Fe_2O_3$powder.

### 3.2 FTIR study:

The FTIR spectrum of $Fe_2O_3$ powder is shown in Fig. 2. Characteristic absorption bands at 536.57 $cm^{-1}$ and 460.09 $cm^{-1}$ for powder are assigned to $Fe_2O_3$. From the IR data, there is no evidence that $Fe_2O_3$ are contaminated by foreign materials in the system.

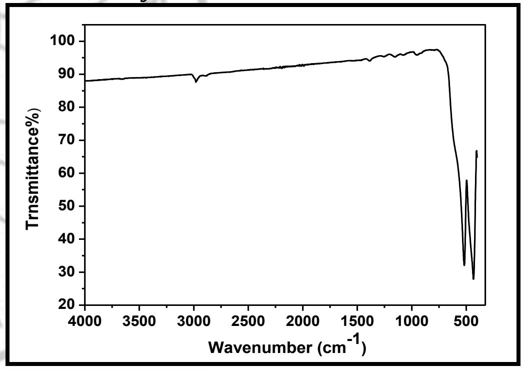

**Fig. 2** FTIR spectrum of $Fe_2O_3$ powder

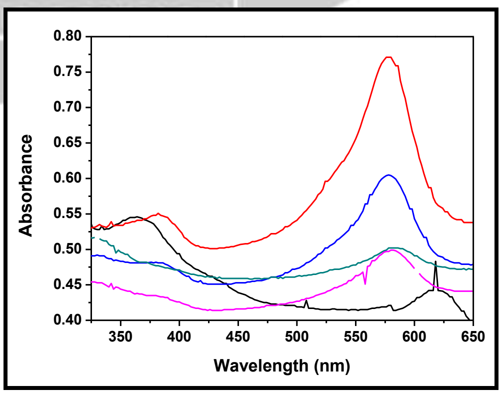

**Fig. 3** Photodegradation of malachite green by $Fe_2O_3$ sintered at 700°C.

### 3.3 Photodegradation of malachite green (MG):

The effect of time on the photocatalytic activity of the $Fe_2O_3$ photocatalyst for the degradation of MG diluted in distilled water under UV-light irradiation is shown in Fig. 3. The sample irradiated at 20 min shows maximum activity for MG. A further comparison reveals that more than 75% of malachite green decomposes within 20 min of irradiation.

## Conclusion

1. **$Fe_2O_3$ was synthesized by innovative synthesis route, i.e. auto-combustion synthesis.**
2. **Thermal stability of oxide was carried out by TG/DTA, which indicate oxide stable at 700°C.**
3. **FTIR results indicate the phase formation of oxide material.**
4. **As prepared $Fe_2O_3$ material exhibited good photocatalytic activity towards the malachite green.**

## References:

1. Hoffmann MR, Martin SC, Choi W, Bahnemann DW. Chem Rev 1995;(95) 69
2. Ehrhardt H, Campbell SJ, Hofmann M. Scr Mater 2003;(48) 1141
3. Klimkiewicz Roman, Wolska Jolanta, Preepiera Aleksander, Przepiera Krystyna,Jablonski Maciej, Lenart Stanislaw. J Mater Res Bull 2009;(44)15
4. Deng H, Li XL, Peng Q, Wang X, Chen JP, Li YD. Angew Chem Int Ed 2005;(44)2782
5. Kundu Animesh, Upadhyay C, Verma HC. Phys Lett A 2010 (311) 410
6. Yao CW, Zeng QS, Goya GF, Torres T, Liu JF, Wu HP. J Phys Chem C 2007(111) 274
7. Qiu J, Wang C, Gu M. Mater Sci Eng B 2004(112)111
8. Yuan ZH, Zhang LD. J Mater Chem 2001;(11) 1265
9. Kobayashi M, Shirai H, Nunokawa M. Ind Eng Chem Res 2002(41) 903

# Study of Activity of H-ZSM-5 Catalysts for Light Alkane Aromatization

Raviraj S. Kamble[*, 1], N. Viswanadham[2], Tanaji S. Patil[1], Vijay P. Kothavale[1], Rajan S. Kamble[1]
[1] Bhogawati Mahavidyalaya, Kurukali, Tal. Karveer, Dist. Kolhapur
[2] Indian Institute of Petroleum, Mohkampur, Dehradun
* Corresponding author (ravikam11@gmail.com)

## Abstract

**Nanocrystalline mesoporous ZSM-5 (MZ) and micrometer range normal ZSM-5 (NZ) were synthesized. The organic template was used in MZ synthesis. The materials MZ and NZ were characterized for XRD, acidity and micicropore volume. Improvement in pore volume along with mesoporosity was observed in MZ. The MZ exhibited relatively lower acidity, but has greater amount of strong acidity when compared to NZ. The catalysts were tested for their activity towards light alkane aromatization using n-hexane and cyclohexane as feedstock. The increase in the aromatics and hence the octane boosting was observed significantly in case of MZ catalyst owing to improved mesoporosity in it.**

**Keywords**
**Nanocrystalline, ZSM-5, mesoporosity, octane boosting, aromatization**

## 1. Introduction

Zeolites are finding more industrial applications by virtue of their properties such as thermal stability, shape selectivity and the flexibility in tailor-making of catalyst for various reactions [1, 2]. Presence of uniformly distributed micropores in the zeolites provides high surface area and excellent shape selectivity [3, 4]. Y zeolite in fluid catalytic cracking (FCC), mordenite in n-paraffin isomerization, and ZSM-5 in light alkane aromatizaton are some of the well-known industrial applications of zeolites [5-7]. However, the hydrothermally synthesized zeolites need to be modified to improve their properties especially for thermal stability, porosity and acidity before their use for catalytic applications. Steaming or acid treatment or combination of both treatments is generally used for the modification of zeolite properties [8]. The treatments facilitate removal of aluminum from the crystalline framework followed by its wash out by acid leaching to make more silicious zeolite. The type and severity of treatments needed for a zeolite depends on the zeolite types and the reaction to be catalyzed. In case of mordenite, the dealumination is used mainly for opening of the side pockets and for the creation of mesopores to improve the diffusion of bulky branched products [9, 10]. For ZSM-5, the purpose is to improve its acidity as well as porosity [11]. Desilcation by post synthesis alkali treatment of silicious zeolites was also observed to create extra-porosity [12]. However, the materials obtained by such treatments may have limitations due to the presence of persistent extra-framework aluminum species in the narrow zeolite channels and structural damage of the framework at severe dealumination conditions [13, 14]. The properties of the materials are also not reproducible at many times. Hence, it is recommended to tailor the zeolite properties during synthesis instead of its post synthesis modifications. Much work is done in the area of synthesizing large pore zeolites and high surface area mesoporous materials for obtaining the materials of improved porosity. But the industrial applications of these mesoporous materials are yet to be proven due to their lower thermal stability and weak acidity [15, 16,]. Creation of mesoporosity in zeolites such as ZSM-5 during hydrothermal synthesis is of much interest due to its wide applications in the petroleum, petrochemical and fine chemical industries. More recently, a new carbon templating method has been introduced for creation of mesoporous voids in zeolites after the calcinations [17]. However, the method was reported to consume high amount of carbon material and limitations in incorporation of aluminum into the framework [18]. Grieken et al. reported the effect of synthesis parameters on the crystallinity and crystal size of the ZSM-5 [19]. The almost striking option for obtaining mesoporosity could be the systematic decrease of the crystal size from micro domain range to nano scale domain size so as to obtain intercrystalline mesoporosity.

It is well known that ZSM-5 based catalysts are generally used for the aromatization of light alkanes such as n-propane, n-butane, n-pentane and industrial feedstocks containing light paraffins such as natural gas liquid (NGL) and light naphtha (LN). Catalytic aromatization of lower alkanes is of great importance since this expands the raw material base for the production of aromatics. The demands for the aromatization processes will grow with increasing pressure for effective utilization of crude oil by producing highly valued and highly marketable products from rather low valued readily available in excess in refineries. Many authors reported ZSM-5 as good catalyst for aromatization (agata). Viswanadham et al. studied the effect of the dehydrogenating component of H-ZSM-5 and Zn/H-ZSM-5 catalysts on n-heptane aromatization reaction [20]. Nguyen et al. studied Due to the shape selective properties of ZSM-5 zeolite BTX (benzne, toluene, xylenes + ethyl benzene) are predominantly present in the aromatic fractions (agata itself).

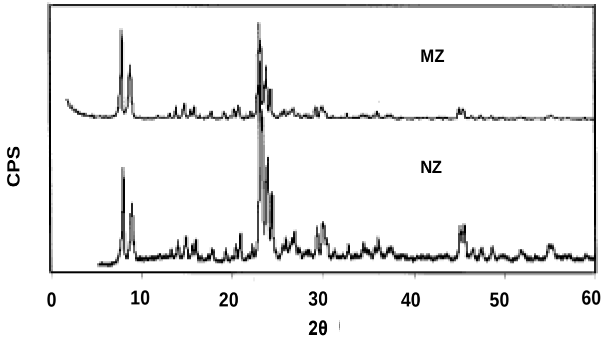

**Fig. 1 X-ray diffraction patterns of ZSM-5 samples**

The present study is aimed to synthesize nano meter range ZSM-5 crystals with improved porosity, where detailed characterization studies such as surface area, external surface area, pore volume, micropore volume and mesoporosity were conducted to understand the properties of the new material. A comparative study of mesoporous and normal ZSM-5 was done. Both the catalysts were tested for the light alkane conversion to investigate the effect of particle size on the catalytic activity.

## 2. Experimental

### 2.1 Synthesis of ZSM-5

In both the synthesis methods described below, it was aimed to produce ZSM-5 in which the framework Al was in the fixed amount equivalent to an atomic Si/Al ratio of 30. In the synthesis of micrometer, ZSM-5 (NZ) the procedure followed was given in patented literature [21] and for nano-sized (mesoporous) ZSM-5 (MZ) the procedure given by Van Grieken et.al. was followed [19].

### 2.1.1 Synthesis of Normal ZSM-5 (NZ)

In this synthesis Sodium silicate (Merck) was used as silica source. Sodium hydroxide was added slowly to sodium silicate solution and after that Al source ($Al(NO_3)_3$, Merck) and then template Tetrapropyl ammonium hydroxide (TPAOH, Merck) was added drop wise. The components were mixed with constant stirring at room temperature. The pH of the resulting gel was then adjusted to 10.5 by adding 1:1 $H_2SO_4$ solution before charging it in Teflon lined autoclave for hydrothermal synthesis at 180 $^0$C for 3 days. The product thus formed was filtered and washed with deionised water

### 2.1.2 Synthesis of Mesoporous ZSM-5 (MZ)

In this synthesis Tetraethyl orthosilicate (TEOS, Merck) was used as silica source. $Al(NO_3)_3$ (Merck) was used as Al source, whereas TPAOH was used as template. The batch composition used was of molar ratio $Al_2O_3$ : 60 $SiO_2$ : 21.4 TPAOH : 650 $H_2O$. Tetrapropyl ammonium hydroxide (TPAOH, Merck) was used as structure directing agent and template. After adding all the ingredients the solution was left to hydrolyze at room temperature for 41 hours on magnetic stirrer. The gel thus obtained was heated at 80 $^o$C to evaporate water and to obtain a concentrated gel. The concentrated gel was filled in a Teflon lined autoclave (200 ml) for hydrothermal synthesis. The synthesis was performed at 170 $^oC$ for duration of 48 h. Recovery of solids from this highly stable suspension was obtained by centrifuging at a very high speed (12000 rpm).

### 2.2. Reaction studies

The aromatization reactions, namely n-hexane conversion and cyclohexane conversion were conducted for measuring aromatization activity of catalysts. All the reactions were conducted at 723 K, 10 bar pressure, 6 $h^{-1}$ WHSV feed flow rate and $N^2$/HC molar ratio of 2.

## 3. Results and Discussion

The powder X-ray diffraction patterns of the samples are shown in Fig. 1. The samples exhibited the typical XRD patterns of ZSM-5 framework structure. The XRD peaks of the two samples NZ and MZ shown in Fig. 1 reveal characteristic differences. In MZ the peaks are broader and largely attenuated whereas in NZ they are sharp. However both XRD patterns depicted exhibit a very low background signal and sharp reflections indicating excellent crystallinity of both the samples. The decrease in peak intensity and increase in line width in case of MZ can be attributed to decrease in crystal size.

Table 1 contains textural properties of zeolites. Significant difference in the properties of NZ and MZ samples was observed, where the sample MZ exhibited the higher surface area and pore volume. The BET surface area of NZ and MZ were 345.7 $m^2/g$ and 461.1 $m^2/g$ respectively. The higher external surface area values of MZ (138.2 $m^2/g$) when compared to NZ (89.9 $m^2/g$) was observed in the present study. It can be explained by the possible formation of nanosized ZSM-5 particles in the MZ sample. The decrease in crystal size is also evident from the very large increase in external surface area. The total pore volumes of the corresponding samples NZ and MZ are 0.1763 $cm^3/g$ and 0.3855 $cm^3/g$ respectively. The pore volume exhibited by NZ is in agreement with the literature findings. The higher pore volume of MZ could be due to the increase in micropore, mesopore and macropore volumes. However, a careful analysis of the pore volume data indicated that the major increase in pore volume in MZ is due to the presence of pores with diameter > 500 Å, followed by the pores with diameter 20-500 Å.

Table 1 shows total acidity and strong acidity of both the samples. NZ exhibited higher total acidity (0.79 mmol $NH_3$/g) than MZ which was having 0.42 mmol $NH_3$/g . However, the strong acid sites were found higher in case of MZ. In NZ strong acid sites were 0.05 mmol $NH_3$/g whereas MZ possessed 0.16 mmol $NH_3$/g strong acid sites. These strong acid sites are very useful for any solid acid catalyst to carry out conversions.

The comparison of products on MZ and NZ using n-hexane and cyclohexane as feed is given in Table 2. The conversion was found to be more on MZ (98%) than NZ (94%) in case of n-hexane LPG was formed higher on MZ (44.5 wt.%) as compared to NZ on which LPG gas produced was 39.2 wt.%. The increase in isoparaffins was significant on both the catalysts. It indicated the formation of isomers through two possible steps (i) isomerization which seemed to be less significant due to the absence of metallic function and (ii) through cracking into smaller fragments and alkylation of small alkanes and alkenes like propane/propene etc. The olefin content in the product on NZ was 11.9 wt.% where as it was 2.8 wt.% on MZ. On NZ and MZ, 5.8 wt.% and 14.9 wt.% aromatics were obtained respectively. It indicated the hydrogen transfer reactions were favoured over MZ than NZ. The RON was found to be increased on both the catalysts. The RON of n-hexane is 24.8. Thus the gain in RON was more on MZ (69.5) as compared to NZ (41.33). It was indeed due to the presence of high aromatics content in the products.

The naphthene cyclohexane was also used as feed to understand the reaction pathways for the aromatization reaction. MZ exhibited higher conversion (96%) while NZ gave 92% conversion as shown in Table 2. The LPG production was maximum on MZ (41.0 wt.%) as compared to NZ which gave 36.4 wt.% of LPG. However in case of cyclohexane, isoparaffins formed over both the catalysts were less as compared to that of n-hexane. The olefin content in the product of catalysts MZ and NZ were 4.7 wt.% and 6.0 wt.% respectively. Both the catalysts exhibited significant increase in the aromatics content which was much higher as compared to that of n-hexane. The catalyst MZ and NZ showed 32.9 wt.% and 26.7 wt.% of aromatics respectively. The dehydrogenation of formed naphthenes was favoured over MZ to give high yield of aromatics. Thus it appeared that MZ exhibited superior catalytic activity in the aromatization reaction.

**Table 1 Catalytic Properties of NZ and MZ samples**

| Sr No | Properties | NZ | MZ |
|---|---|---|---|
| 1 | BET Surface area ($m^2/g$) | 346 | 461 |
| 2 | External Surface area ($m^2/g$) | 90 | 138 |
| 3 | Pore volume (cc/g) | 0.18 | 0.39 |
| 4 | Micropore volume (cc/g) | 0.10 | 0.13 |
| 5 | Total acidity (m mol $NH_3$/g) | 0.79 | 0.42 |
| 6 | Stong acidity (m mol $NH_3$/g with DH > 100 kJ/mol) | 0.05 | 0.16 |

**Table 2 Product yields in n-hexane and cyclohexane conversion**

| Hydrocarbon composition (wt.%) | n-Hexane (Feed) | | Cyclohexane (Feed) | |
|---|---|---|---|---|
| | Product on NZ | Product on MZ | Product on NZ | Product on MZ |
| Conversion (%) | 94 | 98 | 92 | 96 |
| Fuel gas ($C_1$+$C_2$) | 1.5 | 0.6 | 2.7 | 2.0 |
| LPG($C_3$+$C_4$) | 39.2 | 44.5 | 36.4 | 41.0 |
| $C_{5+}$ Paraffins | 15.0 | 6.5 | 5.2 | 5.3 |
| Isoparaffins | 21.4 | 27.3 | 8.1 | 7.3 |
| Olefins | 11.9 | 2.8 | 6.0 | 4.7 |
| Naphthenes | 4.1 | 0.5 | 12.5 | 5.8 |
| Aromatics(Benzene) | 5.8 (0.4) | 14.9 (1.1) | 26.7 (1.2) | 32.9 (1.8) |
| Others | 1.1 | 2.9 | 2.4 | 1.0 |
| Total | 100 | 100 | 100 | 100 |
| RON | 66.13 | 94.3 | 97.2 | 102.8 |

## 4. Conclusion

**TEOS method can be employed for obtaining the ZSM-5 of improved porosity with increase in zeolitic pores as well as the creation of mesopores. The physicochemical properties of ZSM-5 depend on the crystal size and these clearly differentiate nanocrystalline material from microcrystalline material. When the catalyst was tested for catalytic activity, it was found that the presence of mesopores in ZSM-5 can dramatically boost the octane number of light alkane feedstocks by facilitating hydrogen transfer reactions between olefinic intermediates and cyclic intermediates to obtain enhanced yields of aromatics and LPG. This catalyst enables the process more effective for the light alkane upgradation in terms of product quality and economics.**

## References

[1] H. L. Hoffman, Hydroc. Proc. 67 (2) (1987) 41.
[2] W. HÖlderich, M. Hesse, F. Naumann, Angew. Chem. Int. Ed. Encl. 27 (1988) 226.
[3] A. Hollo, J. Hancsok, D. Kallo, Appl. Catal. A: Gen. 229 (2002) 93.
[4] N.Y. Chen, W. E. Garwood, Catal. Rev. Sci. Eng. 28 (2&3) (1986)198.
[5] M. A. Camblor, A. Corma, A. Martinez, F. A. Mocholi, J. P. Pariente, Appl. Catal. 35 (1987) 299.
[6] N. Viswanadham, J. K.Gupta, L. Dixit, M.O.Garg, J. Mol. Catal. 258 (2006) 15.
[7] N. Viswanadham, G. Muralidhar, T. S. R. Prasada Rao, J. Mol. Catal. 223 (2004) 269.
[8] J. Scherzer, ACS Symp. Ser. 248 (1984) 157.
[9] N. Viswanadham, Manoj Kumar, Micropor. Mesopor. Mater. 92 (2006) 31.
[10] M. J. A. van Tromp, M. T. Garriga Oostenbrink, J. H. Bitter, K. P. de Jong, D. C. Koningsberger, J. Catal., 190 (2000) 209.
[11] J. L. Molz, H. Heinichen, W. F. HÖlderich, J. Mol. Catal. A: Chem. 136 (1998) 175.
[12] J. C. Groen, J. C. Jansen, J. A. Moulijn, J. Pe`rez-Ramirez, J. Phys. Chem. B 108 (2004) 13062.
[13] N. Viswanadham, N. Ray, and T.S.R. Prasada Rao, Stud. Surf. Sci. Catal. 113 (1998) 433.
[14] Z. H. Luan, C. F. Cheng, H. Y. He, J. Klinowsky, J. Phys. Chem. 99 (1995) 10590.
[15] A. Corma, M. S. Grande, V. Gonzalez Alfaro, A.V. Orchilles, J. Catal. 159 (1996) 375.
[16] J. Schmidt, A. Boisen, E. Gustavssion, K. Stahl, S. Pehrson, S. Dahl, A. Carlsson, C. J. H. Jacobsen, Chem. Mater. 13 (2001) 4416.
[17] F. A. Topsoe, C. J. H. Jacobson, M. Brorson, C. Madsen, F. Schmidt, U.S. Patent 6,241, 960, 1999.
[18] T. Schmidt, Inorg. Chem., 39 (2000) 2279.
[19] R. Van Grieken, J. L. Sotelo, J. M. Menéndez, J. A. Melero, Micropor. Mesopor. Mater. 39 (2000) 135.
[20] N. Viswanadham, A. R. Pradhan, N. Ray, S. C. Vishnoi, U. Shankar, T. S. R. Prasada Rao, Appl. Catal. A : Gen. 137 (1996) 225.
[21] R. J. Argauer, G. R. Landolt , US. Patent 3,702,886, 1972.

# Structural and Optical Study of Titanium Dioxide Thin Films by Chemical Spray Pyrolysis

V.P. Kothavale[a], T.S.Patil[a], R.S.Kamble[a], C.M. Kanamadi[b], C. H. Bhosale[c]
a. Bhogawati Mahavidhyalaya Kurukali-416001.
b. Devchand College, Arjunnagar-591237
c. Electrochemical Materials Laboratory, Department of Physics, Shivaji University, Kolhapur-416004, India, Corresponding author: E-mail: vijaypkothavale@gmail.com, Mob.No.: +91 9960233229.

## Abstract:

**Titanium dioxide ($TiO_2$) nanoparticles are deposited onto glass/FTO substrates at optimized substrate temperature 450°C by using a simple chemical spray pyrolysis technique. The $TiO_2$ thin films are characterized for their structural, morphological optical and photoelectrochemical properties using photoelectrochemical (PEC), XRD, SEM and UV-vis spectrophotometer. The PEC study shows that, both short circuit current ($I_{sc}$) and open circuit voltage ($V_{oc}$) are ($I_{sc}$ = 0.62 mA and $V_{oc}$ = 430 mV) relatively higher at 450°C substrate temperature. Films are polycrystalline in nature with tetragonal crystal structure. SEM study gives the films are compact, dense and uniform in nature. The observed direct band gap is about 3.4 eV for typical films prepared at 450° C.**

**Keywords: Nanostructures; Semiconductors; Thin films; Surface properties.**

## 1. Introduction:

$TiO_2$ is a wide band gap, chemically stable and environmental friendly semiconductor with good biocompatibility and stability. It occurs in three phases namely anatase (< 550 $^{\circ}$C), rutile (> 550 $^{\circ}$C) and brookite (>1200 $^{\circ}$C). $TiO_2$ film has the unique characteristics such as high optical transmittance over the wide wavelength range and excellent adhesion to the substrates. The $TiO_2$ thin films are used in variety of applications such as dye-sensitized solar cells, antireflection (AR) coatings, and photocatalytic activity [1-2].

Many researchers have used several methods for depositing the $TiO_2$ thin films viz. sol–gel [3-5], chemical vapor deposition [6,7], evaporation [8], sputtering [9-11], pulsed laser deposition [12], electrodeposition [13], and spray pyrolysis [14-21]. Amongst these deposition methods, the most widely studied one is the spray pyrolysis technique. It is simple, commercially available, cost-effective for mass production with excellent control of chemical uniformity, and stoichiometry. The properties of spray-deposited $TiO_2$ thin films depend on a type of precursor used, because of their thermal decomposition behavior. The precursors like titanyl acetyl acetonate (TiAcAc) [$TiC_{10}H_{14}O_5$], Ti $(i\text{-}OC_3H_7)_4$, 2-propanol, titanium tetrachloride ($TiCl_4$), titanium (IV) isobutoxide [Ti $((CH_3)_2CHCH_2O)$], peroxo-titanium complex solution, etc. have so far been reported [14–21], for the deposition of $TiO_2$ thin films of good quality. The titanium tetraisopropoxide (TTIP) has been used to prepare $TiO_2$ thin films by spray pyrolysis [22]. Jung et al. [23] deposited titanium dioxie ($TiO_2$) thin films using sol-gel method and titanium (IV) iso-propoxide $Ti\{OCH(CH_3)_2\}_4$ as precursor. It is found that Plasma treated $TiO_2$ showed excellent photocatalytic activity on phenol and toluene under UV light irradiation. Oh et al [24] synthesized the nanophase $TiO_2$ thin films from (TTIP) by a sol-gel dip-coating method and studied the effect of calcinations temperature on the photoactivity of the $TiO_2$ films. Cleveland et al [25] deposited the $TiO_2$ thin films using Atomic layer deposition (ALD) from (TTIP). Wang et al [26] reported the Titanium oxide nanoparticles using the low-pressure spray pyrolysis (LPSD) of titanium tetraisopropoxide (TTIP) and also gives the possible mechanism of particle formation in the LPSP process.

The attempts are going on to improve photoelectrochemical performance of $TiO_2$ thin film for their photocatalytic properties. In the present work $TiO_2$ thin films are synthesized by using spray pyrolysis technique by using Titanium isopropoxide $Ti\ \{OCH(CH_3)_2\}_4$ as a precursor and photoelectrochemical (PEC) technique was used to optimize the substrate temperature.

## 2. Experimental

Titanium (IV) iso-propoxide $Ti\{OCH(CH_3)_2\}_4$, was dissolved in ethanol at room temperature. The resulting 100 ml of 0.1M solution was sprayed onto cleaned corning glass substrates maintained at different substrate temperatures ranging from 400 °C, at interval of 50 $^0$C to 500 $^0$C. The fine aerosols of the solution sprayed through an atomizer undergo pyrolytic decomposition onto the preheated glass substrates forming $TiO_2$ thin films. Other preparative parameters like, spray rate (4ml/min) and nozzle to substrate distance (32 cm) were kept constant for all the experiments.

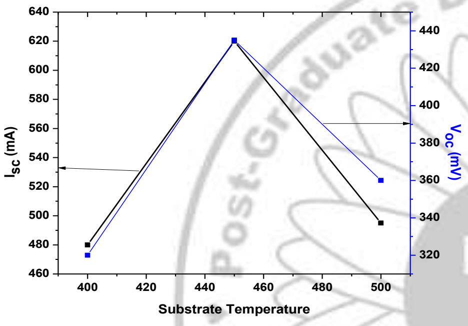

**Fig.1** Variation of $I_{sc}$ and $V_{oc}$ with substrate temperatures for $TiO_2$ thin films. (On FTO)/0.1NaOH/C PEC solar cell.

Photoelectrochemical (PEC) cell was fabricated using the two-electrode configuration system, comprising $TiO_2$ thin film as a photoanode and graphite as a counter electrode, with the 0.1 M NaOH as an electrolyte. The cell was illuminated with 20 W UV OMNILUX lamp with an excitation wavelength of 365 nm for the measurement of short circuit current ($I_{sc}$) and open circuit voltage ($V_{oc}$). The structural characterization of deposited $TiO_2$ thin films was carried out, by analyzing the X-ray diffraction patterns obtained under Cu-Kα radiation from a Bruker AXS, Model: D2 Phaser. Transmission spectra were recorded at room temperature using a UV-1800 Shimadzu, UV spectrophotometer and surface morphology was studied using JEOL JSM-6360, Japan scanning electron microscope (SEM).

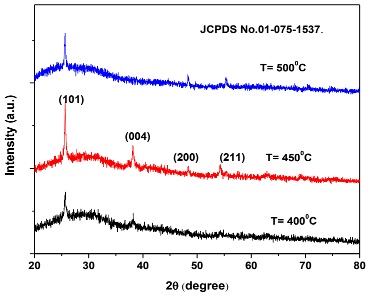

**Fig.2** X-ray diffraction patterns of $TiO_2$ thin films.

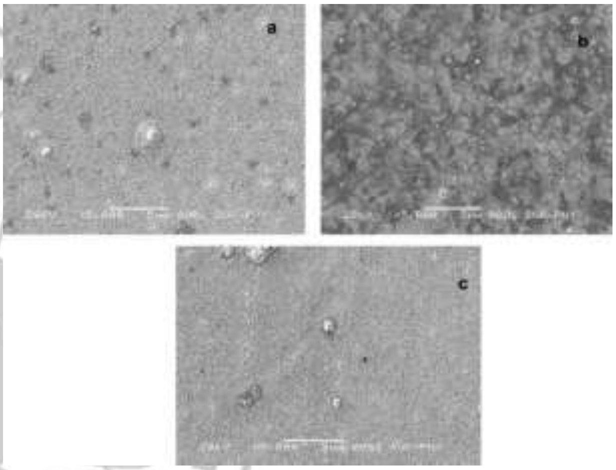

**Fig.3(a-c)** SEM images of $TiO_2$ thin film

## 3. Results and discussion

### 3.1 Photoelectrochemical (PEC) studies

The optimization of preparative parameters of good quality $TiO_2$ thin films is carried out with PEC technique. These preparative parameters are optimized by taking relatively maximum values of short circuit current ($I_{sc}$) and open circuit voltage ($V_{oc}$) of the PEC cell formed with $TiO_2$ working electrode. Fig.1 shows the variation of short circuit current ($I_{sc}$) and open circuit voltage ($V_{oc}$) as a function of substrate temperature. The graph shows both $I_{sc}$ and $V_{oc}$ values increase with increase in substrate temperature and attain maximum values $I_{sc}$= 0.62 mA and $V_{oc}$= 430 mV for the film deposited at 450°C temperature and then decrease for further increase in substrate temperature. In this case the higher values of $I_{sc}$= 0.62 mA and $V_{oc}$= 430 mV are obtained because of variation in the stoichiometry with respect to substrate temperature.

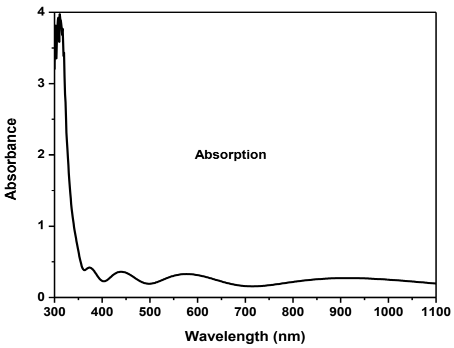

**Fig. 4(a) 4 (a**) Optical absorption spectra of $TiO_2$ thin films

### 3.2 X-ray diffraction studies

Fig.2 shows the X-ray diffraction patterns of $TiO_2$ thin films deposited at different substrate temperatures. The films are nanocrystalline and fit well with the tetragonal crystal structure with most intense (101) plane and well match with JCPDS card No. 01-075-1537. Some weak reflections such as (004), (200), (211), (204) have also been observed. The reason for comparatively lower peak intensities is due to the lower film thickness, incomplete growth of film and formation of amorphous plus nanocrystalline phase in thin films. As the substrate temperature increases, crystallinity of the films increases upto 450°C. Further increase in substrate temperature decreases peak intensity and it is attributed to the lower thickness of the films. The crystallite size of the deposited thin films was calculated by using Scherrer's formula

$$D = \frac{0.9\lambda}{\beta \cos \theta} \qquad (1)$$

Where, $D$ is the crystallite size, $\beta$ is the broadening of the diffraction line measured at half of its maximum intensity (FWHM) and $\lambda$ is the X-ray wavelength (1.5405A˚). The average crystallite size increases from 50 nm.

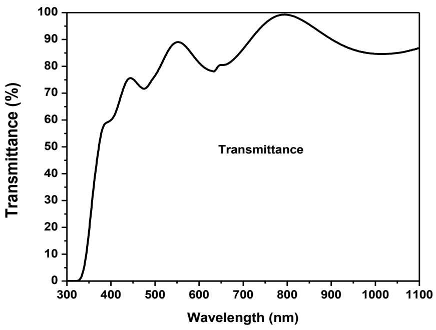

**Fig. 4(b)** Optical transmittance spectra of $TiO_2$ thin films

### 3.3 Morphological properties

Fig. 3(a-c) shows the scanning electron micrographs of $TiO_2$ thin films deposited at various substrate temperatures. It is seen that films are uniform, compact, having randomly distributed. Such kind of morphology is useful for use of $TiO_2$ electrode in photocatalysis

### 3.4 Optical properties

The optical absorption and transmission spectra of $TiO_2$ films deposited at various substrate temperatures are shown in fig. 4 (a) and (b) respectively. The films show moderate optical transmittance between 90 to 95 % at 550 nm. The thickness was measured using Steller Net Inc USA spectroscopic reflectometer having UV–Vis light source with CCD detector. The thickness of the $TiO_2$ film deposited at 450 °C is 480 nm. Fig. 4(c) shows the plots of $(\alpha h\upsilon)^2$ Vs $h\upsilon$ of $TiO_2$ thin films deposited at 450° C substrate temperatures. Band gap of film deposited at 450 °C is 3.4 eV This value of band gap energy is slightly greater than the value of energy reported for single crystal $TiO_2$ [27] and comparable with earlier reported value for spray deposited $TiO_2$ thin films [28].

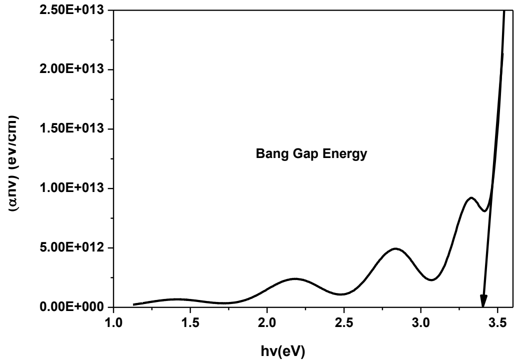

**Fig. 4(c)** Plot of $(\alpha h\upsilon)^2$ Vs hυ of $TiO_2$ thin film.

## 4 Conclusions

**Well adherent semiconducting $TiO_2$ thin films can be deposited using a simple chemical spray pyrolysis technique. The effects of substrate temperature on to the PEC, structural and optical properties of titanium dioxide thin films have been investigated. The films are polycrystalline in nature with tetragonal crystal structure. The SEM study reveals that the films are uniform, compact, having randomly distributed. Band gap energy is 3.4 eV.**

## Acknowledgement

One of the authors (V. P. Kothavale) is very much thankful to the Prof. C. H. Bhosale, Department of Physics, Shivaji University Kolhapur for providing the experimental facility.

## References:

[1] N.S.P. Bhuvanesh, J. Gopalkrishnan , J. Mater.Chem.7 (1997) 2297.
[2] A.L. Linsebigler, G. Lu, J.T. Yates Jr , Chem. Rev. 95 (1995) 735.
[3] C.J. Brinker, M.S. Harrington , Sol. Energy Mater. 5 (1981)159.
[4] G.S. Vicente, A. Morales, M.T. Gutierrez , Thin Solid Films 391 (2001)133.
[5] Q. Fan, B. Mc Quillin, A.K. Ray, M.L. Turner, A.B. Seddon, J. Phys. D Appl. Phys ,332 (2000) 683.
[6] G.A. Battiston, R. Gerbasi, M. Porchia, A. Morigo, Thin Solid Films 239 (1994)186.
[7] D.J. Won, C.H. Wang, H.K. Jang, D.J. Choi , Appl. Phys. A 73 (2001) 595.
[8] P. L Obl, M. Huppertz, D. Mergel , Thin Solid Films 251 (1994) 72.
[9] L. J. Meng, M.P. dos Santos ,Thin Solid Films 226 (1993) 22.
[10] N. Martin, C. Rousselot, C. Savall, F. Palmino , Thin Solid Films 287 (1996)154.
[11] K. Okimura, Coat. Technol.135 (2001) 286.
[12] M.P. Moret, R. Zallen, D.P. Vijay, S.B. Desu , Thin Solid Films 366 (2000) 8.
[13] L.Kavan, M.Gratzel , Electrochim. Acta 40 (1995) 643.
[14] W.W. Xu, R. Kershaw, K. Dwight, A. Wold , Mater. Res. Bull. 25 (1990) 1385.
[15] L. Castaneda, J.C. Alonso, A. Ortiz, E. Andrade, J.M. Saniger, J.G. Banuelos, Mater. Chem. Phys. 77 (2003) 938 -944.
[16] M.O. Abou-Helal, W.T. Seeber, Appl. Surf. Sci. 195 (2002) 53.
[17] C. Natarajan, N. Fukunaga, G. Nogami, Thin Solid Films 322 (1998) 6.
[18] S. Zhang, Y.F. Zhu, D.E. Brodie, Thin Solid Films 213 (1992) 265.
[19] K.D. Rogers, D.W. Lane, J.D. Painter, A. Chapman, Thin Solid Films 466 (2004) 97.
[20] M. Okuya, N.A. Prokudina, K. Mushika, S. Kaneko , J. Eur. Ceram. Soc.19 (1999) 903.
[21] N. Golego, S.A. Studenikin, M. Cocivera, T. Joshep, J. Mater. Res.14 (1999) 698.
[22] L. Andronic, A. Duta, Thin Solid Films, Volume 515, Issue 16 (2007) pp. 6294–6297.
[23] C.K. Junga, T, I.S. Bae, Y.H.Song, T.K.Kim, J. Vlcek, J. Musil, J.H.Boo, Surface & Coatings Technology 200 (2005) 534– 538.
[24] S. H. Oh, J. S. Kim, J. S. Chung, E. J. Kim, S. H. Hahn, Chem. Eng. Comm., 192 (2005) 327–335.
[25] E. R. Cleveland, L. H. Lecordier, G. W. Rubloff , J. Vac. Sci. Technol. A 30 Jan (2012) (1).
[26] W. N. Wang , I. W. Lenggoro, Y. Terashi, T. O. Kimc, K. Okuyama, Mater. Sci. and Engg. B 123 (2005)194–202.
[27] A. B. Haugen, I. Kumakiri, C. Simon, M.A. Einarsrud, Journal of the Eur. Cer.Soc.31 (2011) 291–298.
[28] S. Valencia, J. M. Marín and G. Restrepo, Mater. Sci., 4 (2010) 9-14.

# Natural cellulosic fiber as a Humidity Sensor

Vidya Kalyankar[1],Mahesh Salunkhe[2], Prashant More[2], Heena Meroliya, Sharada Dagade[2]
Shobha A.Waghmode[1]*
1Department of Chemistry MES Abasaheb Garware College, Pune-411004
2 Deapartment of Chemistry , Y.M.College Bharati Vidyapeet, Pune 411038
Email Id – *shobhawaghmode@yahoo.co.in

## Abstract-

**The objective of this study is related to humidity sensing ability of cellulosic natural fibers with high response towards moisture absorption. Natural fiber is naturally antibacterial, UV-protective and biodegradable. The variety of cellulose samples we have used is Baggasse of sugarcane containing 41-44% of cellulose and the type of cellulose is α-Cellulose from the method of extraction. It is a polydispersed linear polymer of β-(1, 4)-D-glucose units so the advantage is taken of hydrophilic Hydroxyl (–OH) groups on surface of extracted α-Cellulose fiber which can detect moisture by interaction through Van der Waal's forces. All three fibre samples were characterized by Fourier transformer infrared spectroscopy (FTIR), Thermo gravimetric analysis (TGA). Finally fibers were tested for Humidity sensor properties.**

**Key word – Humidity sensor, Cellulosic natural Fiber, TGA, FTIR.**

## 1. INTRODUCTION

Cellulosic fiber is one of the most important part of the biomass and most abundant, renweable, economically cheap sourse available in nature[1]. Cellulose is major framework of natural fiber which provides strength,stability to the fiber. It allows moisture absorption from atmosphere which can be quantitised using sensors[2,3].The study of water vapor concentration in air is important but critical because it may affect the business cost of the product, health and safety of the personnel [4]. It also influences various physical, chemical, and biological processes hence humidity sensing is very important, especially in the control systems for industrial processes and human comfort.

In this work we explored humidity sensing properties of natural cellulosic fibres like sugar cane baggasse fiber , bamboo , maize and raw almond. These sources are very economical,ecofriendly, with good moisture absorption properties and relatively good thermal stability. Future prospects of this work are better as these sources as well as sensor circuit used will prove to be cost effective.

## 2. EXPERIMENTAL

### *Raw materials :*

Sugarcane baggasse fiber sample was collected from Pune district (Western Maharashtra, India).The chemical reagents used for treating these fibre samples and preparing cellulose were analytical grade purchased from sigma-aldrich.

### *Preparation of cellulose from raw fiber*

First all fiber samples were cut into small pieces and grind using a cutting mill. Isolation of cellulose from other surface impurities like hemicellulose, lignin from raw fiber sample was achieved by alkali treatment and bleaching followed by sonication. The samples were soaked in 4 wt% NaOH solution for 2 days at room temperature and then washed with deionised water to get neutral pH 7 followed by bleaching treatment using 5 wt% NaoCl solution. After bleaching samples were washed with deionised water till pH becomes neutral and then dried under vaccum[6,7]. The synthetic methods were used for extraction removes not only surface impurities such as wax, oil, lignin layer but also it helps to reduce its size. This increases effective fiber surface area and it gives uniform surface for better adhesion. This method helps to improve moisture sensing ability of fibres as the fibres are sensitive towards humidity

### *C.Sensor fabrication*

Fiber were fabricated on glass epoxy PCB (printed circuit board) to increased its contact realibilty and to get more stable resistnace. electrical contacts were made using silver paste.

### *D .Experimental set-up*

Experimental used for sensor testing is depicted in figure 1.For humidity sensing the sensing sample, Humidity sensor and detector aligned properly, as shown in Fig.1. Humidity is exposed on the film which is kept inside the dome and the resistance is measured as a function of relative humidity (% Rh) on Detector which is kept outside of the dome. The detector output is connected to the high resistance electrometer (KEITHLEY 6517B). The humidity was created by passing water vapour in the test chamber. When fiber has shown stable reading, the saturated vapours were wiped by tissue paper and chamber was kept at its original position without disturbing alignment. The chamber was dehumidified by using dryimg agent like phosphorous pentoxide ($P_2O_5$), calcium carbonate, silica gel, etc. The sensitivity is the change in output resistance per unit change in Rh%.

**Fig 1**: Experimental set-up

### CHARACTERIZATION:

All three samples were characterised by using FTIR spectroecopy, TGA followed by humidity sensor application.

### *FTIR Spectroscopy*

These samples were characterized by FTIR (Perkin-Elmer) with thickness variation (0.35 mm, 0.19 mm).

Examination of changes in chemical composition of cellulosic fibre before and after exposure to humidity was recorded. Spectrum was obtained in the range of 250 to 4500 $cm^{-1}$ in transmission mode.

### *Thermo gravimetric analysis*

The thermal properties of all three cellulosic fibers were conducted by means of thermo gravimetric analysis using TGA instrument across range of 30-$400^0$C.

### *Humidity Sensor analysis*

The Humidity Sensing properties of fiber is carried out by means of Humidity Sensor. The variation of relative humidity is kept from 100-30% Rh. The resistance is measured with varying relative humidiy. Also,same experiment were repeated with thickness variation of fibers.

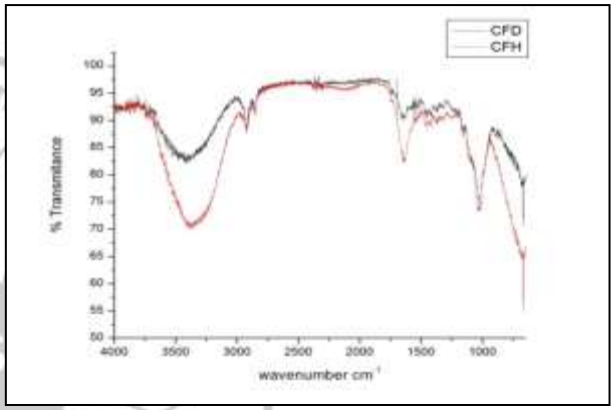

**Fig 2:** CFD – cellulosic fiber before moisture absorption , CFH- cellulosic fiber after exposed to the humidity(Bamboo)

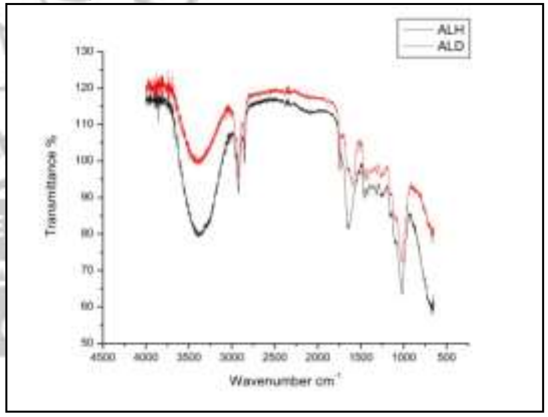

**Fig 3:** ALD- almond fiber before moisture absorption, ALH-almond fiber after moisture absorption

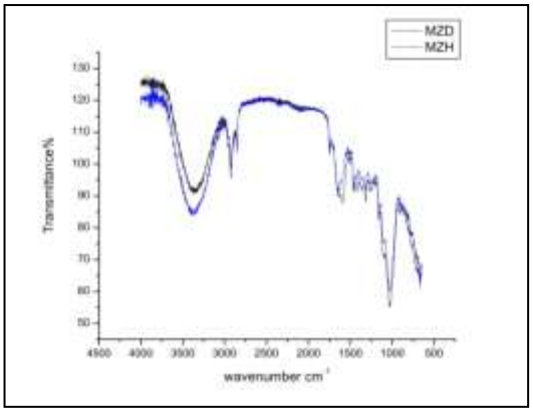

**Fig 4:** MZD- maize fiber before thermo gravimetric analysis moisture absorption, MZH- maize fiber after moisture absorption.

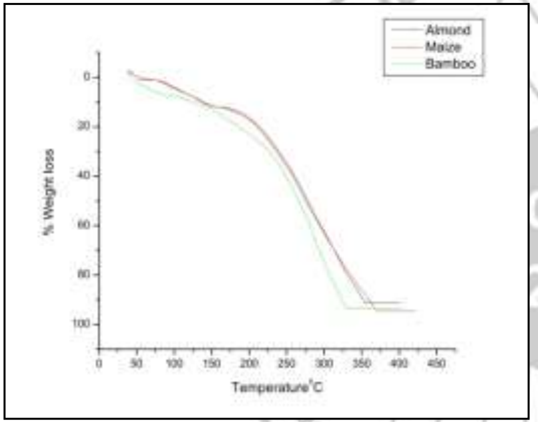

***Fig 5:** TGA curves for sugarcane,, Maize and Bamboo fiber*

## 3. RESULT AND DISCUSSION:

*FTIR Spectroscopy*

The chemical changes in fiber due to moisture absorbance were analysed using FTIR spectroscopy. The increased –OH concentration is evident from the increased intensity of the peak between 3300-3500 cm$^{-1}$ bands compared to unexposed sample to humidity[13,15]. Also, decreased in peak between 1200-1300cm$^{-1}$ shows lignin removal and increased intensity of peak around 1000cm$^{-1}$ in all spectra's are evidence of increased cellulose content where -C-O-C-pyranose ring skeletal vibration leads to prominent peak[8,9]

*Thermo gravimetric analysis*

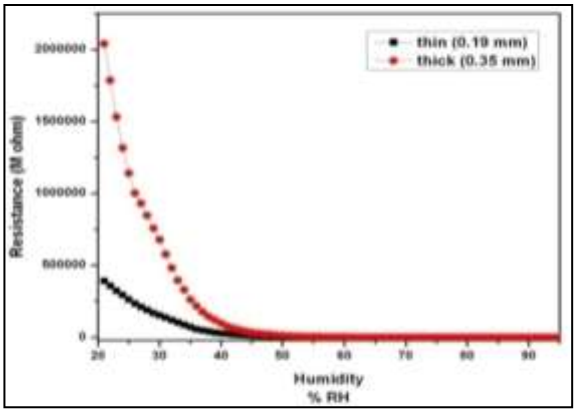

TGA analysis shows initial weight loss started at 60-70$^0$C which is attributed to evaporation free water molecule in samples. A shoulder peak begins at around 200$^0$C followed by decomposition peak at 300$^0$C which suggest there are 2 degradation peaks[14].

**Fig 6:** Response of Sugarcane fiber to humidity change with thickness variation

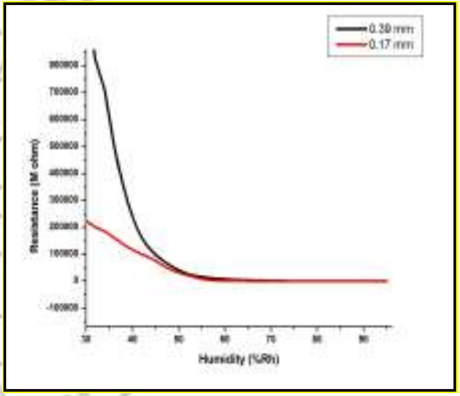

**Fig 7:** Response of almond fiber to humidity change with thickness variation.

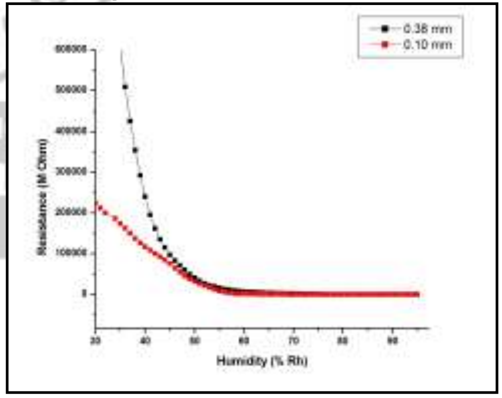

**Fig 8:** Response of maize fiber to humidity change with thickness variation.

Weight loss at 200$^0$C is due to decomposition of hemicelluloses and lignin[1,10]. Then dominant peak at 300$^0$C shows pyrolysis of cellulose. From this analysis we conclude that all three fiber samples are stable in second TGA step around

$210^0$C. all these three samples as a humidity sensor are applicable till this temperature.

*Humidity Sensor*

Sugarcane fiber shows 28.296 MΩ resistance at 43.5%Rh,Maize 168.970 MΩ resistance at 37.5% Rh, Almond 178.870 MΩ resistance at 40.5% Rh (relative humidity) room humidity at room temperature. It changes its resistance when it is exposed to higher humidity that is 100%Rh. As we increase the relative humidity, resistance decreases which shows fiber is highly sensitive towards humidity. Also response time is about 45-90seconds (Bamboo),30-45 seconds(Maize), 35-55 seconds(Almond) and recovery time is 2-3 minutes for bamboo, 1-2 minutes for maize and 1-2 minutes for almond.

The decrase in resistance is because of the saturation of cellulosic fiber by adsorbtion of water molecules on its surface. One more reason is that the formaion of more water layer on the surface of fiber by physisorbtion leads to self ionisation of water molecule in $H^+$,$OH^-$ ions. The protons are dominant carriers for electrical conductivity when sensor exposed to humidity tends to decrease in resistance.

## CONCLUSION :

**Sugarcane fibers are applicable as a novel humidity sensor evidenced by FTIR spectroscopy with increased intensity of –OH concentration. Thermal stability of all these fiber sensors is upto $210^0$C. sensor study of fibers shows that fibers are more sensitive towards lower humidity and less sensitive toward high humidity. Also,comparison between all three samples shows that the almond fiber is less sensitive than other two samples with less recovery time of ~1-2 minutes.**

## ACKNOWLEDGEMENT :

The authors are grateful to the ISRO-SPPU-STC program for financial funding of this research work also to the Center for sensor studies, and Dr.R.C.Aiyer and Pooja More, Savitribai Phule pune univeristy for technical guidance during present research work.

## REFERENCES:

1. Huu Dat Nguyen, Thi Thanh Thuy mai, Ngoc Bich Nguyen, Thanh Duy Dang, My Loan Phung Le,Than Tai Dang and Van Man Tran 2013 Advances in natural sciences: Nanoscience and Nanotechnology
2. E.Abraham, B.Deepa, LA.Pothan, M.Jacob, S.Thomas, U.Cvelbar, R.Anandjiwala 2011 carbohydrate Polymers 86 1468-1475
3. M.M.Kabir, H.Wang, K.T.Lau, F.Cardona 2012 Composite: Part B 43 2883-2892
4. Christian, S new 2002 Generation of humidity sensors sens Rev 22, 300-302
5. Madhavi V. Fuke, Anu Vijaya, Milind Kulkarni, Ranjit Hawaldar,R.C Aiyer,2008 Talanta 76 1035-1040.
6. Das M, Chakraborty D 2008Journal of applied polymer science 107 522
7. Bhattacharya D, Grminario L T, Winter W T 2008 carbohydrate polymer 73 371
8. Elanthikkak S, Gopalkrishnapanicker U, Varghese S and Guthrie J T 2010 Carbohydr. Polymers 80,852.
9. Kaushik A and Singh M 2011 Carbohydr. Res 346,76.
10. Li R, Fei J, Cai Y, Li Y, Feng J and Yao J 2009 carbohydr. Polymers 76, 94.
11. Mu-Rong Yang, Ko-Shao Chen, Sensors and Actuators B 49 (1998)
12. B. C Yadav, Anchal Srivastava, R. K. Shukla & G.CDubey, Indian journal of pure and applied physics, 44, 2006.
13. Lojewska J,Miskowiec P, Lojewski T, Pronienwicz L.M. 2005 polymer degradation and stability 88 512-520
14. Yang,Yan,Chen,Dong,Zheng 2007 Fuel 86 1781-1788
15. Doan TTI, GaoSL,mader E 2006 composite science technology

# Influence of Ruthenium doping on Structural Properties of $MoO_3$ Thin Films

[1]D. S. Sutrave, [2]V. L. Mathe, [3] P.S.Joshi [4]S. D. Gothe
[1]D.B.F Dayanand College of Arts and Science, Solapur, Maharashtra 413003
[2] Physics Department, Savitribai Phule Pune University, Pune, Maharashtra 411001
[3] Walchand Institute of Technology, Solapur, Maharashtra 413003
[4]Sangameshwar College, Solapur Maharashtra 413003

## Abstract

**The present work examines the effect of Ru doping on $MoO_3$ thin films on steel substrate deposited by Sol-gel spin coat method. The annealing temperature was $600^0$C for pure $MoO_3$ and $800^0$C for Ru doped thin films. The doping concentration of Ru was varied from !0% to 50%. The influence of Ru doping on structural and morphological properties of $MoO_3$ thin films were studied. The XRD revealed that all films are highly crystalline in nature with monoclinic phase for molybdenum peaks. On the doped XRD pattern some new peaks were observed and are matched with ruthenium orthorhombic phase indicating an incorporation of dopant in pure molybdenum oxide.**

## 1. Introduction

For the last several years, molybdenum oxide has attracted attentions because of their potential applications in gas sensing devices[1-2], optically switchable coatings[3] and catalysis[4] etc. It also exhibits electrochromism, photochromism after intercalating with an appropriate cation (such as Li+, Na+) making suitable for use in display devices[5], smart windows[6] and electrochemical storage[7]. Such a wide range applications is due to the non-stoichiometric nature of molybdenum oxide and to the occurrence of different phases of molybdenum oxide such as α-$MoO_3$, $MoO_2$, β-$MoO_3$, etc. The crystal structure of $MoO_2$ is monoclinic while α− $MoO_3$ and β− $MoO_3$ have orthorhombic and monoclinic structure respectively. The dependence of electrical property on oxygen concentration is such that $MoO_3$ is optically transparent[8] and electrically insulating in nature.

In order to deposit $MoO_3$ thin film, number of methods have been adopted, such as electro-deposition[9], thermal evaporation[10] pulsed laser deposition, hot wire chemical vapour deposition[11], magnetron sputtering method[12], Sol-gel and Spray Pyrolysis etc. In the present work, we reported our investigations on structural and morphological properties of molybdenum oxide $MoO_3$ and Ru doped $MoO_3$ thin films deposited by Sol-gel spin coat method.

## 2. Experimental

### 2.1 Synthesis

. $MoO_3$ solution was prepared by dissolving Ammonium Molybdate Tetrahydrate with appropriate proportion in double distilled water. Once the solution became transparent, then drops of isopropyl alcohol were added as a solvent and the mixed solution was stirred on magnetic stirrer at $50^0$C for 240min and aged for 24 hours to yield a clear and viscous solution which was ready for sol gel spin coat deposition. The doped solution was prepared by adding to the precedent solution Ruthenium Trichloride as a dopant source. The weight percentages of Ru were 10%, 20%, 30%, 40% and 50%. The solution became clear and homogeneous after stirring for 240min at $50^0$ to $70^0$C on magnetic stirrer and aged for 24 hours to obtain viscous solution.

### 2.2 Deposition

Before deposition, the steel substrates were polished with zero grade polish paper and washed with double distilled water in an ultrasonic bath for 15 minute. To deposit the film by spin coat method, few drops of gel are placed on the steel substrate, which is then rotated at high speed (3000rpm) in order to spread the fluid by centrifugal force. The film thickness can be adjusted by varying the rotation speed, the rotation time, and the viscosity of the gel. After deposition, films were annealed under furnace. The annealing temperature for pure molybdenum film was $600^0$C and Ru doped molybdenum films was $800^0$C

## 3. Result and Discussion

### Structural Analysis by XRD

The structural analysis was performed by using Bruker D8 Advanced instrument with source CuKα1 with λ =1.5406. The 2θ angle is varied from $20^0$ to $90^0$. Fig. 1(a), (b), (c), (d), (e) and (f) shows the XRD patterns of pure $MoO_3$ and Ru doped $MoO_3$ thin films which were deposited on the steel substrates. All samples exhibited crystalline nature. The XRD patterns showed peaks for the planes [002], [311], [020], [111], [220] and [011] were matched with $MoO_3$ phase of molybdenum oxide with monoclinic structure. The peaks for plane [002] and [311] were observed in only pure molybdenum sample. Remaining peaks for the plane [111] and [020] were observed in all the samples whereas, the dominating peak with plane [011] was disappeared after 20 wt % Ru doping. Some peaks with plane [011], [211], [220], [031] and [202] were also observed in the XRD patterns of doped thin films which were matched with $RuO_2$ phase with orthorhombic structure.

All peaks were matched with JCPDS card No. 89-1554, and 88-0323 for $MoO_3$ and $RuO_2$ respectively. The lattice constants ‘a, ‘b’ and ‘c’ for $MoO_3$ and $RuO_2$ peaks are calculated from the XRD data. It shows good agreement with the standard values (a=7.122Å, b=5.366Å, c=5.566Å) in JCPDS-89-1554 and (a=4.486Å, b=4.434Å, c=3.093Å) for $MoO_3$ and $RuO_2$ respectively. The effect of doping concentration on the values of lattice constants is shown in the graphical form in fig. 2 and 3.

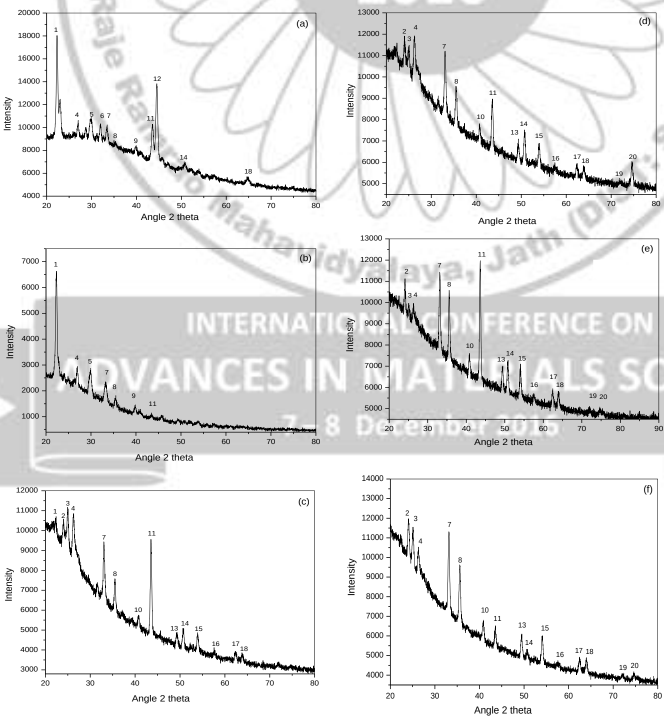

**Fig. 1 XRD patterns of (a) $MoO_3$, Ru doping with (b), 10%, (c) 20%, (d) 30%, (e) 40% and (f) 50%**

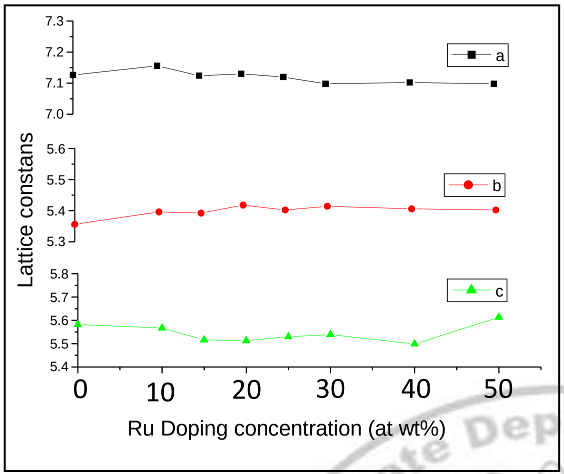

**Fig. 2 Variation in lattice constants of $MoO_3$ peaks with doping concentration**

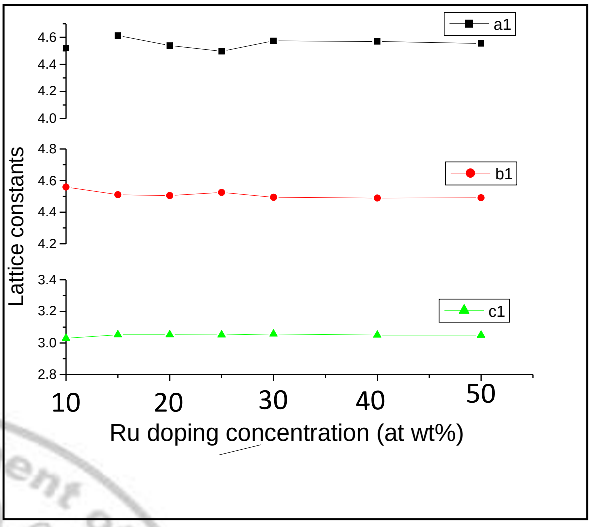

**Fig. 3 Variation in lattice constants of $RuO_2$ peaks with doping concentration**

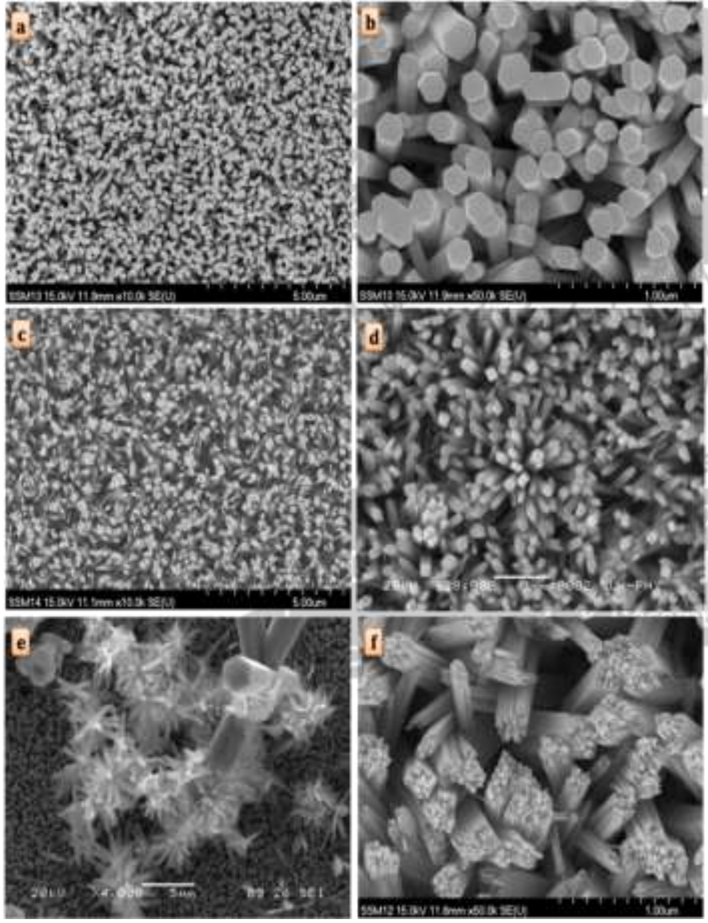

**Fig. 3**(a to f) Shows SEM image of ZnO, $TiO_2$, and $TiO_2$- ZnO nanostructure samples.

## 4.Conclusion

**Ru doped $MoO_3$ thin films were prepared with different values of Ru content by the sol-gel spin coating method. The diffraction patterns reveal a good crystalline behaviour for all the films with the monoclinic and orthorhombic phase for $MoO_3$ and $RuO_2$ diffraction peaks. As a result Ru incorporation has a strong effect on structural properties of $MoO_3$ thin films.**

## References

1. J. Okumu, F. Koerfer, C. Salinga, M. Wutting, J. Appl. Phys. 95, 7632 (2005).
2. S. H. Mohamed, O. Kappertz, J.M. Nagaruiya, T. P.L. Pedersen, R. Drese, and M. Wutting, Thin solid Films 429 ,135 (2003).
3. J. Okumu, F. Koerfer, C. Salinga, T. P. Pedersen, M. Wutting, Thin Solid Films 515, 1327 (2006).
4. W. Zhang, A. Desikan, and S. T. Oyama, J. Phys. Chem. 99, 14468 (1995).
5. R. J. Colton, A. M. Guzman, and J.W. Rabalais, J. Appl. Phys. 49, 409 (1978).
6. J. N. Huiberts, R. Griessen, J. H. Rector, R. J. Wijngaarden, J. P. Dekker, D. G. DeGroot, and N. J. Koeman, Nature (London) 380, 231 (1996).
7. Mai. L, Hu. B, Chen. Y, Lao. C, Yang. R, Dai.Y, and Wang. Z, DOI: 10.1002/adma.200700883 (2007)
8. C. Jullien, A. Khelfa, O.M. Hussain and G. A. Nazri, J. Crystal Growth, 156, 235 (1995).
9. Patil. R. S, Uplane. M. D, Patil. P. S, Appl. Surf. Sci“, 252, 354-358 (2006)
10. Sian. T. S and Reddy. G. B, Journal of Applied Physics, vol. 98, 2, Article ID 026104 (2005)
11. Hsu. C. S, Chan. C.C, Peng . H, Hsu. W. C, Thin Solid Films, vol. 516, no. 15, pp. 4839–4844 (2008) , Appl. Surf. Sci, 257, 2074 (2011)

# Green Synthesis of ZnO nanoparticles using plant extracts

Sunil D. Kumbhar,[a] Sunil B. Patil,[a] Mahesh G. Kukade,[a] Anita J. Bodake*[a]
[a]Department of Chemistry, Rajaram College, Vidyanagar, Kolhapur-416004( MS)
*[a] corresponding author: anitabodake07@gmail.com

## Abstract:

**Development of green nanotechnology is generating interest of researchers toward eco-friendly synthesis of nanoparticles. In the present study, stable zinc nanoparticles are synthesized using plants extract of *Holarrhena pubescence seeds* and *Acanthocereus tetragonus* leaves extract. The nanoparticles are characterized using X-ray diffraction, Fourier Transformed Infra-Red spectroscopy, Scanning Electron Microscopy, UV-Visible spectroscopy and Energy Dispersive Spectroscopy. The comparative results of synthesis were reported as H-ZnO and A-ZnO. It is observed that the morphology is well controlled in H-ZnO as compared to A-ZnO. Percentage composition of Zn and O in H-ZnO and in A-ZnO is studied by EDS analysis.**

**Keywords: ZnO nanoparticles, *Holarrhena pubescence and Acanthocereus tetragonus.***

## Introduction:

Nanoparticles are of great scientific interest, and they represent a bridge between the bulk materials and the molecules. Earlier, the nanoparticles were studied because of their size-dependent physical and chemical properties but now they have entered in commercial exploration with huge applications. The intrinsic properties of metal nanoparticles are due to their size, composition and morphology (Dickson & Lyon 2000). These nano size metal oxides have been attracted researchers by their ability to withstand under harsh condition and safe to mankind (Fu *et al.* 2005). ZnO nanoarticles are among the top most photocatalysts which are used in disinfecting waste water and to decompose pesticides, herbicides. Biosynthesis of ZnO nanoparticles and their use in various fields are reported by many authors (Bagabas *et al.* 2013, Malarkodi *et al.* 2013).

Green synthesis of nanoparticle are cost effective, easily available, eco friendly, nontoxic, large scale production and act as reducing and capping agent as compared to the chemical method which is a very costly as well as it emits hazardous by product which can have some deleterious effect on the environment. Biological synthesis utilizes naturally occupying reducing agent such as plant extract, microorganism, enzyme, polysaccharide which are simple and viable which is the alternative to the complex and toxic chemical processes. Plants can be described as nano factories which provide potential pathway to bioaccumulation into food chain and environment. Among the different biological agents plants provide safe and beneficial way to the synthesis of metallic nanoparticle as it is easily available so there is possibilities for large scale production apart from this the synthesis route is eco-friendly, the rate of production is faster in comparison to other biological models such as bacteria, algae and fungi .

Different deposition techniques at different condition grows different morphologies of ZnO. Due to variation in surface morphology ZnO is common for various application. It is necessary to find more simple ways to synthesis ZnO metal nanoparticle with less hazardous materials.In the present work, seed extract of *Holarrhena pubescence* (**Figure 1**)and leaves extract of *Acanthocereus tetragonus (***Figure 2***)* were used to synthesis ZnO nanoparticles.

**Figure 1: *Holarrhena pubescence***

**Figure 2: *Acanthocereus tetragonus***

**Figure 3.** *XRD pattern of H-ZnO and A-ZnO*

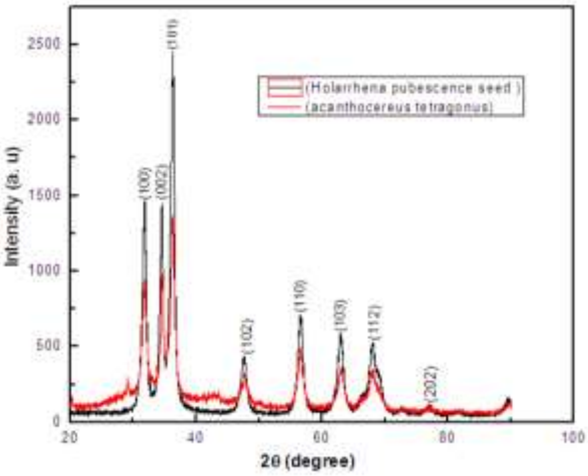

**Figure 4:** *UV-Vis Spectra*

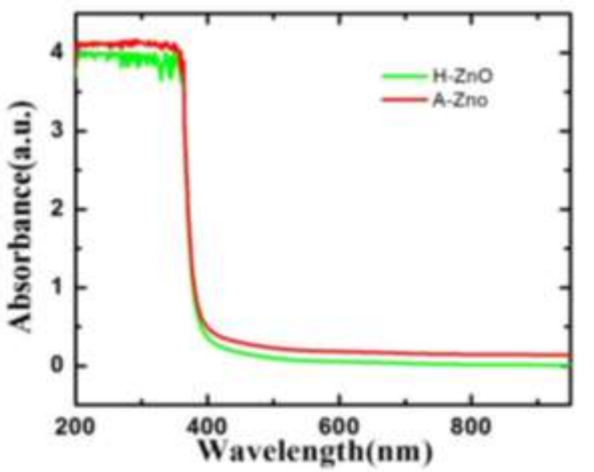

## Experimental:

In the present synthesis, zinc acetate dehydrate and sodium hydroxide of analytical reagent grade were purchased from Sigma Aldrich. Precursors solutions were prepared in doubled distilled water. Initially prepared extract of *Holarrhena pubescence* seed by soxhlet extractor and *Acanthocereus tetragonus* prepared by crushing leaves in distilled water were used. In these extracts Zinc Acetate was added. NaOH solution was added after 1hr in both flasks with constant stirring at 333K to maintain pH 10-11. Residue was filtered and dried under IR lamp. Dried powders were annealed at 573 K for 8 hour. White color powder of both sample were further characterized by XRD, SEM, UV-Vis, and EDS. Slurry of ZnO nanoparticle prepared in polyvinyl alcohol (PVA) and coated on glass substrate by doctor blade method.

## Result and Discussion:

Synthesized and annealed powder of A-ZnO and H-ZnO were studied by X-ray diffraction technique for the determination of crystal structure along with structural changes and identification of phases. **Figure 3** shows the XRD patterns of the H-ZnO and A-ZnO, respectively. The crystallite size for H-ZnO is 14 nm and A-ZnO is 13nm. The intensity of all peaks decreases relatively in A-ZnO than H-ZnO.

Optical energy band gap of H-ZnO and A-ZnO powdered was estimated using UV-Vis-NIR Spectrophotometer (Shimadzu UV-3600) in the wavelength range 200–950 nm. **Figure 4** shows the optical band gap values which are found to be 3.2 eV and 3.3 eV respectively. Increment in band gap energy can be ascribed to larger grain size of A-ZnO than H-ZnO. The reactive free surfaces are offered by oxygen vacant ZnO owing to improved adsorption of gas molecules.( L. Polavarapu *et al* 2015)

**Figure 5:** ***SEM image of H-ZnO (a,b) and A-ZnO (c,d) H-ZnO,A-ZnO (magnification 10000X and 60000X)***

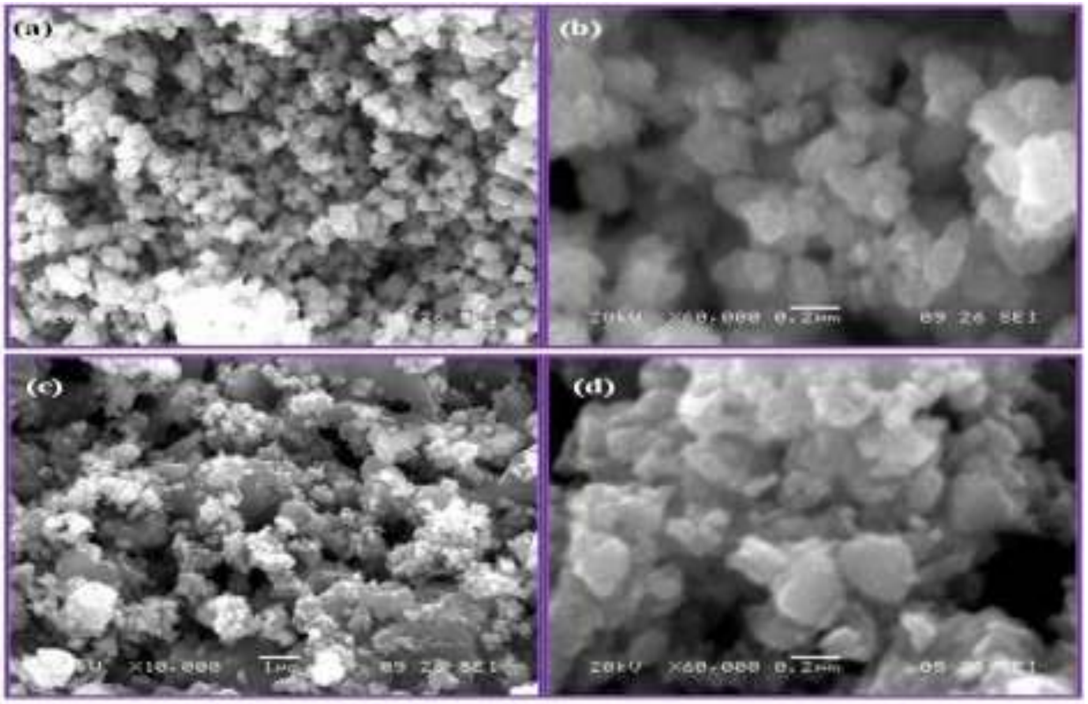

SEM images of H-ZnO and A-ZnO at two different magnifications are revealed in **Figure 5** . Globular particulate of H-ZnO and A-ZnO distributed over the entire surface. The formation of globular particulates is more regular in H-ZnO than A-ZnO due to homogenous nucleation. Organic content like different phenolic groups, flavonoides etc in plant cape and controls the growth of ZnO nanoparticle (S. Iravani 2011). This type of morphology is more useful for enhancing gas response.

Energy Dispersive X-ray Spectra (EDS) of H-ZnO and A-ZnO were observing atomic percentage of Zn and O in H-ZnO is 81.42% and 18.58% whereas in A-ZnO it is 38.72% and 61.28% respectively. Sample of H-ZnO is shows atomic percentage of ZnO is more than A-ZnO.

**Conclusion:**

**This is the first study to develop an efficient protocol for the biosynthesis of ZnO nanoparticles using *Holarrhena pubescence* seeds and *Acanthocereus tetragonus* leaves extract to highlight the eco-friendly approach for commercial application of Zinc nanoparticles in agriculture as nano-biofertilizers, in the field of medicine and in field of gas sensors.**

## References:

1. Dickson RM & Lyon LA .*Journal of Physical Chemistry* 104: **(2000)** 6095–6098.
2. Fu L, Liu Z, Liu Y, Han B, Hu P, Cao L & Zhu D *Advanced Materials* 7: **(2005)** 217–221
3. Bagabas A, Alshammari A, Aboud MFA & Kosslick H *Nanoscale Research Letters* 8(1): 5**(2013)** 16
4. L. Polavarapu, S. Mourdikoudis, I. Pastoriza-Santos and J. Pérez-Juste , *Cryst. Eng. Comm*, **17** (**2015**), 3727
5. S. Iravani, *Green Chem.*, 13,(**2011**), 2638

# Magnetoelectric Studies On Nanocrystalline BST-CNFMO Composites

M. M. Sutar, Birajdar, A.N. Patil
S. M. Dr. Bapuji Salunkhe College, Miraj (INDIA)
*Email: smilind20066@gmail.com

## Abstract

**$Ba_{1-x}Sr_xTiO_3$ (BST) is a ferroelectric material possessing Tc in the vicinity of room temperature ~ $30^0$C. The Tc is observed to vary between $30^0$C to $60^0$C for x varying between 0.20 to 0.30 respectively. As crystal structure is unstable near Tc, investigations on BST based ME composites for x=0.30, 0.25 and 0.20 may provide useful information in terms of physics of Magnetoelectric effect. To determine a composition possessing the high value of $\rho_{dc}$, $M_s$, μ, λ and low value of $H_c$, initially CNFMO was synthesized for x = 0.00, 0.10 0.20, 0.30 and 0.40 and investigated for determination of above mentioned physical parameters. It is observed that x=0.30 posses optimum values of the parameters and therefore x= 0.30 was selected as a magnetostrictive phase. The paper reports investigations on ME composites formed with $Ba_{1-x}Sr_xTiO_3$ (x=0.20, 0.25 and 0.30) and $Co_{0.9}Ni_{0.1}Fe_{1.7}Mn_{0.3}O_4$ (CNFMO) ferroelectric and magnetostrictive systems. The BST as well as CNFMO is synthesized via hydroxide co-precipitation route to achieve particle size in nanoscale range. The paper reports the linear and quadratic magnetoelectric coefficients α and β. It is observed that the α and β are maximum for y=0.30 as expected for the ME composites, while α and β is observed to follow dependence as predicted by the relationship**

$$\alpha = dE/dH = (\Delta V_0)/G*d*(\Delta h) \text{ and } \beta = (\Delta V_0)/2*d*h*(\Delta H)$$

**Keywords: Magnetoelectric, Magnetodielectric Composites.**

## 1. Introduction

Barium strontium titanate (BST), Barium Lanthanum titanate (BLT), Barium Neodemium titanate (BNT) systems showing their strong response to the applied AC/DC electric field. This property is very attractive and has been used to develop microwave devices such as phase shifters, tunable capacitance etc.$Ba_{1-x}Sr_xTiO_3$ is a well-known ferroelectric material where the transition temperature ($T_c$) could be reduced nearly from 120 ºC down to -231 ºC by varying x between 0 to 1. The compounds with x in the vicinity of 0.30 are of special interest owing to its $T_c$ = 30 ºC (≈RT) and very high value of dielectric constant (ε) in the vicinity of $T_c$ in both ferroelectric and paraelectric regions [2-5]. As far as the Magneto electric(ME) properties are concerned it is expected that ME coefficients will be high in the ferroelectric region and in the vicinity of $T_c$. As the ME phenomenon is proportional to the change of polarization as a function of applied stress, the ME properties are expected to be sensitive to the compositional variations of BST for x varying from 0.20 to 0.30. Here the $T_c$ for x=0.30 is at 30 ºC and increases to nearly 58 ºC for x=0.20. Here $Co_{0.9}Ni_{0.1}Fe_{1.7}Mn_{0.3}O_4$ (CNFMO) ferrite is selected to be a magnetostrictive phase considering its high value of coefficients of magnetostriction (λ).

Further ME properties of the composites are maximum for composition in the vicinity of y=0.5, as the ME properties are governed by the relation (1-y), where y is the fraction of the magnetostrictive phase in the composite. Thus the present paper reports the magnetic, dielectric, ME properties of the CNFMO-BST composites. To form nano particles of individual's phases, both CNFMO and BST powders are synthesized via hydroxide co precipitation route. The paper reports the synthesis and characterization of different CNFMO and BST compositions and composites. The crystal structure and particle size is determined using XRD spectra. The physical properties of CNFMO like dc resistivity ($\rho_{dc}$), initial permeability (μ), saturation magnetization ($M_s$) etc. are determined to arrive at a composition possessing optimally high values of $\rho_{dc}$, $M_s$, λ and low value of $H_c$. Further the paper also reports the dielectric, ME properties of the CNBST composites.

## 2. Experimental Procedure

### A] Synthesis of $Co_{0.9}Ni_{0.1}Fe_{2-x}Mn_xO_4$ (CNFMO)

We have been interested in hydroxide co-precipitation method for the synthesis of series of manganese doped cobalt ferrite with compositions of $Co_{0.9}Ni_{0.1}Fe_{2-x}Mn_xO_4$, where x ranges from 0 to 0.4 because the method ensure ease of preparation, chemical homogeneity at precipitates, purity and uniform grain growth. For good magnetic properties attention is made on sintering temperature, chemical composition and the preparation condition on which the magnetic properties mostly depends. To arrive at a composition possessing the optimal values of ρ, Ms & μ and low Hc, $Co_{0.9}Ni_{0.1}Fe_{2-x}Mn_xO_4$ (CNFM) for x=0, 0.1,0.2,0.3, and 0.4 compositions are synthesized via hydroxide co-precipitation route and are subjected to the measurement of their electric and magnetic properties. The reason for selecting x values from x= 0 to 0.4is that Mn ion being larger in size as compared to iron ion, hence cannot be substituted in crystal structure perfectly beyond x=0.5. The disc compacts were sintering at 1200 °C for 12 h and subsequent furnace cooling to room temperature. The structural characterizations of the samples were done by X-ray diffraction analysis while for complete characterization of these compositions, $\rho_{dc}$ is measured using potential divider arrangement. The physical density ($d_{Bulk}$) is measured using the liquid displacement method while saturation magnetization ($M_s$) is measured using Hysteresis loop tracer from Ms. Arun Electronics, Mumbai (India). The permeability (μ) is measured using a LVDT arrangement and λ is measured using magnetostriction setup.

### B] Synthesis of $Ba_{1-x}Sr_xTiO_3$ (BST)

The $Ba_{1-x}Sr_xTiO_3$ powders are synthesized by employing hydroxide co-precipitation route followed by ceramic process of synthesis for x= 0.20, 0.25 and 0.30. High purity (> 99.9%) Barium acetate [$Ba(CooCH_3)_2$], Strontium nitrate [$Sr(NO_3)_2$], Potassium Titanium Oxalate [$K_2TiO(C_2O_4)_2.2H_2O$] are used as precursors. For complete precipitation of $Ba(OH)_2$ and $TiO(OH)_2$, the molar ratio of KOH to (BaTi) of 1.6 has been used, based on the earlier report [6]. It has been observed that the $Ba(OH)_2$ and $Sr(OH)_2$ is fractionally soluble in water but insoluble in alkaline medium. Therefore the precipitates are washed in dilute $NH_4OH$ solution with pH ~ 10 [7]. The powders are calcined at 1000 ºC for 10 hrs and final sintering is carried out at 1200 ºC for 12 hrs. For characterization of bulk BST, the pellets are also sintered in the same sintering schedule. For further discussion the samples are denoted as BSTx for x=0.20, 0.25 and 0.30.

**Table 1**

| Ferrite CNFMO | ‘a’ Å | Particle size (nm) | ‘$\rho_{dc}$’ $x10^6$ Ω | $d_{Bulk}$ $gm/cm^3$ | $d_{X-ray}$ $gm/cm^3$ |
|---|---|---|---|---|---|
| x=0.0 | 8.18 | 76.80 | 67.1 | 5.38 | 5.69 |
| x=0.1 | 8.23 | 69.37 | 12.92 | 5.29 | 5.58 |
| x=0.2 | 8.25 | 72.27 | 10.76 | 5.03 | 5.54 |
| x=0.3 | 8.29 | 75.05 | 2.236 | 5.01 | 5.46 |
| x=0.4 | 8.30 | 65.17 | 0.145 | 5.00 | 5.54 |

### C] Formation of Composites

The CNFMO and BST composites are formed bearing the formula

$$y\ (CNFMO\ -BSTx)=\ yCNFMO + (1-y)BSTx$$

Where x= 0.20, 0.25 and 0.30 for y=0.30 and 0.40. The sintered powder of CNFMO and BST are grounded together thoroughly using ethanol as a medium in Agot Mortor and pestol. The pellets of diameter 1.2 cm are formed as discussed above. The pellets are sintered at 1200 ºC to form desired ME composites.

The parent compositions CNFMO and BST as well as their composites are investigated for the structural properties using X-ray powder diffractometer (Rigaku Miniflex). For dielectric measurements LCR-Q meter (HP4284A) is used in the frequency range from 100Hz to 1MHz for temperature(T) between RT to 250 ºC for measurement of $C_p$, tanδ as a function of frequency(F), temperature(T) and magnetic field (H) for dielectric and MD characterization of BST and composites. The linear and quadratic magnetoelectric coefficients α and β are determined using a custom designed instrument as reported earlier [8].

## 3. Results and Discussion

The XRD spectra for CNFMO powder for x=0.3 is shown in figure 1(a).It is seen that the observed reflections could be associated with the corresponding hkl planes using standard JCPDS data on $CoFe_2O_4$. Using XRD data, it is observed that CNFMO ferrite possesses the spinal cubic crystal structure with lattice parameter ‘a’ as shown in table1. It is observed that the lattice parameter ‘a’ increases gradually with increasing ‘x’ owing to larger ionic radius of Mn as compared to Fe cations.

Further the particle size is calculated using Scherrer formula and is also shown in table1.

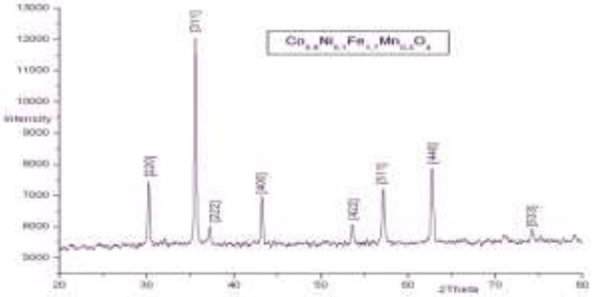

**Figure 1a. XRD spectra for CNFMO(x=0.3)**

From XRD spectra it is observed that all the compositions possess the particle size (D) in the range of 65 to 76 nm. Further the table 1 also shows the magnitude of dc resistivity $\rho_{dc}$, physical density ($d_{Bulk}$), crystalline density ($d_{x\text{-ray}}$), and %porosity (p). It is observed that $\rho_{dc}$ is very high at x=0 and decreases slowly with increasing Mn content. The presence of $Fe^{2+}$ and $Fe^{3+}$ or $Co^{2+}$and $Co^{3+}$ions on equivalent sites is known to cause polaronic conduction in case of ferrites. At very low concentration the Mn and Ni reduce, the percentage of fractional $Fe^{2+}$ and $Co^{2+}$ions formed during the process of synthesis. This causes an increase in resistivity for substitution of Mn/Ni below 0.04 atom percentage [9]. For further increase in Mn/Ni concentration $\rho_{dc}$ decreases slowly with increasing x. The present observations are in confirmation with this report [10]. The magnitude of porosity is as shown in table1. It is observed that the samples are dense and porosity is than 10% comparable with the porosities reported earlier for similar sintering conditions [11].

The figure 1(b) shows the XRD spectra of BST0.25. It is observed that the degree tetragonality (c/a) reduces from 1.0083 to 1.0022 as the x varied from x=0.20 to 0.30 shown in table 2. These results are in confirmation with the earlier report [12]. The magnitudes of 'a' and 'c' are also in confirmation with the A. Ianculescu et.al report. Thus as the x increases, the tetragonality decreases and sample becomes nearly cubic for x >0.30. Using Scherrer's formula the particle size is determined to be between 49 to 65nm (table2). Further, no peak corresponding to any impurity phase is observed in XRD spectra and formation of a pure single-phase composition is confirmed from the observations of the XRD spectra. Figures 2 shows the XRD spectra of CNBST0.25 for y=0.3. The peak corresponding to the reflections of BST and CNFMO could be separately indexed in figure2. No peak corresponding to any impurity phase is recorded in XRD spectra. These observations are sufficient to say that composites are formed as pure biphase system. Figure 3 shows the variation of λ with applied magnetic field (H) for CNFMO series. It is observed that, the λ increases and appears to saturate for H > 4 kOe. The highest value of λ for H=4.5kOe is termed as $\lambda_{sat}$.

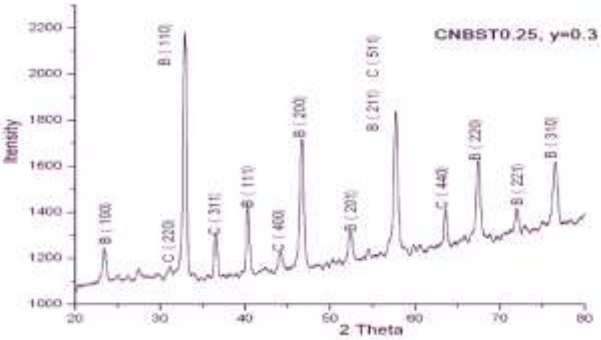

**Table 2**

| Comp. | D(nm) | $T_c$ ℃ | 'a'(Å) | 'c'(Å) | c/a |
|---|---|---|---|---|---|
| BST0.20 | 49 | 58 | 3.920 | 3.95 | 1.0083 |
| BST0.25 | 65 | 42 | 3.824 | 3.84 | 1.0046 |
| BST0.30 | 62 | 30 | 3.809 | 3.81 | 1.0022 |

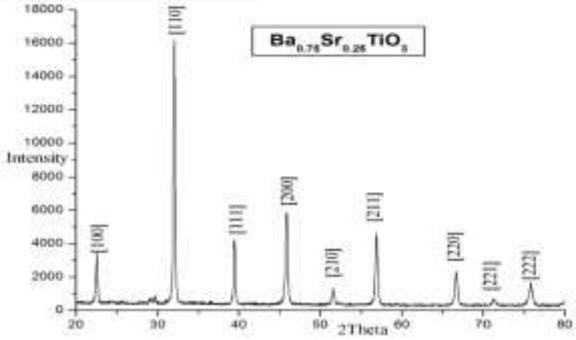

Figure 1b. XRD Spectra for BST0.25

Figure 2. XRD Spectra for CNBST0.25(y=0.3)

**Table 3**

| CNFMO | $M_s$ emu/g | $H_c$ Oe | μ | $\lambda_{sat}$ x$10^{-6}$ |
|---|---|---|---|---|
| x=0 | 141 | 100 | 255 | 115 |
| x=0.1 | 199 | 112 | 502 | 90 |
| x=0.2 | 222 | 112 | 636 | 160 |
| x=0.3 | 252 | 93 | 777 | 167 |
| x=0.4 | 269 | 81 | 911 | 142 |

Table 3 shows the observed magnetic properties of the CNMFO series. From table 3 it is observe that the saturation magnetization ($M_s$) increases with increasing Mn content as expected for Mn substituted cobalt ferrite [10].

This suggests that the majority of Mn ions are present on the A-sites. Further, $H_c$ for all the compositions are closer to 100 Oe and this observation too is in confirmation with the earlier report [13]. It was observed that for substitution of Mn in $CoFe_2O_4$, the $M_s$ increases up to x=0.2 only and decreases for further increasing Mn concentration. On the other hand, the present observations show that $M_s$ increases monotonically for Mn even up to x=0.4. Thus the substitution of Ni at x=0.1 has caused majority of Mn to occupy its preferential A-sites than occupying the B-sites.

Figure 3 Variation of Magnetostriction Coefficient with applied (H).

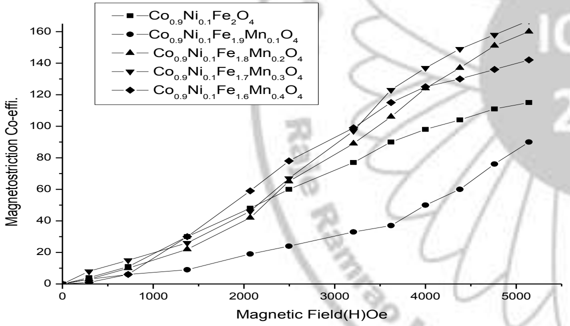

Now figures 4(a) and 4(b) shows variation of dynamic ME coefficients α and β respectively for CNBST composites. Here α represents linear while β represents quadratic ME coefficient defined by the relations as below.

$$\alpha = dE/dH = (\Delta V_0)/G*d*(\Delta h) \text{ and}$$

$$\beta = (\Delta V_0)/2*d*h*(\Delta H)$$

Where $\Delta V_o$ is the r.m.s output voltage developed across the sample in mV , G is the gain of the amplifier, d is the effective thickness of the sample , $h$ is the r.m.s. value of the AC field at frequency 850Hz and $H$ is the imposed DC magnetic field. Further the table3 shows variation of α and β as a function of x and y. It is observed that α is maximum for CNBST0.25 and y=0.4. Similar are the features for variation of β. Here the change in β is insignificant for x=0.25 and x=0.30 and y=0.3 and From the basic theory of ME effect in composites α and β are proportional to y(1-y), where y is the percentage of the piezo-magnetic phase in the composites. Further the α is proportional to piezoelectric coefficient(d),magnetostriction coefficient(λ) magneto-mechanical coupling coefficient($k_m$) and inversely proportional to ε.

## 4. Conclusions

**The present study shows that the CNFMO-BST composite shows ME behavior. Further the magnitudes of the ME coefficients are useful and α is observed maximum at 5.80 mV/cm -Oe for x=0.25, y=0.4. These observations suggest that the compositions studied are interesting in terms of both physics as well as commercial applications.**

## References:

[1] S.A. Gridnev, A.V. Kalgin and V.A.Chernykh, *Integrated ferroelectrics*, 109, 70-75, 2009.

[2] Mark A. McCormick, Ryan K. Roeder and Elliott B. Slamovich, .mater.res.,**16**, No.4,1200-1209,(2001)..

[3] A. Ianculescu, D. Berger, L. Mitoseriu, L. P. Curecheriu, N. Dragan, D. Crisan & E. Vasile, *Ferroelectrics*,**369**, Issue 1,22-34,(2008).

[4] F. zimmerman, M.Voiats, W. menesklou, E.Ivezs-Tiffee, J.Euro.cera.Soci.,**24**(2004), 1729-1733.

[5] A. T. Chien, X. Xu, J. H. Kim, J.Sachleben, J. S. Speck and F. F. Lange,*J.Mater.Res*.**14,**3330(1999).

[6] S.V. Kulkarni, S.S. Veer, D.J. Salunkhe, S.B. Kulkarni and P.B. Joshi, *Mate. Sci. Research India*, **6(2)** 521(2009).

[8] D.J.Salunkhe,S.S.Veer,S.V.Kulkarni,S.B.Kulkarni and P.B.Joshi, *J.Instru.Society*,India,38(4)(2006),294-298.

[9] L.G.Van Uitert, dc resistivity in the Nickel and Nickel Zinc Ferrite System, *J. Chem. Phys*.**23**1883(1955).

[10] J.A. Paulsen, A.P. Ring, C.C.H. Lo, J.E. Snyder, and D.C. Jiles, , *J.Appl.Phys*.**97,**044502(2005).

[11] B.S. Chauhan, R. Kumar, K.M. Jadhav, M. Singh, *J. of Mag. and Mag. Mats*,283 ,71(2004).

[12] A. Ianculescu, D. Berger, L. Mitoşeriu, L. P. Curecheriu, N. Drăgan, D. Crişan & E. Vasile,*Ferroelectrics*,**369**, Issue 122-34 ,(2008).

[13] O.F. Caltun, G.S.N. Rao, K.H. Rao, B. Parvatheeswara rao, Cheol Gi Kim, et.al. *Sen. Letts.5* ,1(2007).

[14] Chang Hyun Kim, Yoon Myung, Yong Jae Cho, Han Sung Kim, Seong-Hun Park, et.al.Electronic, *J. Phys. Chem.C*,**113,** 7085(2008).

[15] Bidaut O, Goux P, Chikech M.K, Belkaoumi M, Manglion M Space charge relaxation in perovskite,*Phys.Rev.B*.49, 7868-7873(1994).

# Synthesis and Characterization of Ruthenium Decorated Reduced Graphene Oxide Nanosheets.

Gaurav Lole, Krishna Daware, Manasi Kasture, Ramchandra Kalubarme, and Suresh Gosavi
Centre for Advanced Studies in Material Science and Solid State Physics,
Department of Physics, Savitribai Phule Pune University, (Formerly University of Pune) Ganeshkhind, Pune - 411007, INDIA, Email: swg@physics.unipune.ac.in

## Abstract

**Graphene is forthcoming as a non-native to the ecosystem but utilitarian to human being. There are incessant processes carried out for graphene synthesis from natural graphite and this is big challenge for mass production of graphene. We have synthesized reduced graphene oxide layered structure by Hummer's method followed by decoration of ruthenium on the layered graphene oxide sheets. The microstructure analysis confirmed the formation and uniform dispersion of Ru on the layered graphene sheets. This RGO sheets are totally comprehensive and useful in combination with transition metals for various applications.**

## 1. Introduction

By exfoliation of graphite, a monolayer obtained i.e. graphene is a one-atom-thick two-dimensional sheet with excellent electrical, mechanical and thermal properties. Bulk production of such quality graphene material is a challenging task for researchers. Lots of efforts was done towards the synthesis of single layer and multi-layer graphene sheets. Chemical vapor deposition, Hummer's method and modified Hummer's method have been most advanced methods used for graphene synthesis. Due to the very high mobility and the possibility to tune the electronic conduction via the field effect, graphene is also a very promising material for future electronic applications[1,2].

Generally graphene oxide is synthesized by Hummer's method, which is the most common and successful method due to its effectiveness and reaction safety. But there are still two drawbacks in Hummers method: (1) the oxidation procedure releases toxic gasses such as $NO_2$ and $N_2O_4$; (2) the residual $Na^+$ and $NO_3$ ions are difficult to remove from the waste water obtained during the synthesis and separation processes employed for GO[1,2,3].

Graphene has come forth as a hopeful material in energy storage and transfer applications due to its high surface area and electrical conductivity. Chemically synthesized graphene has shown extremely higher specific capacitance than conventionally used carbon as electrode materials for supercapacitor application. Graphene sheets derived by reducing graphene oxide (RGO) are also highly active materials towards EDLC application. Additionally, graphene is a perfect substrate for growing nanomaterials to increase capacity and rate performance by facilitating electron transfer for battery or supercapacitor electrode. Interactions with graphene could also help to increase stability over cycling and nanocrystalline morphology of active materials[3,4].

In this study few layered reduced graphene oxide (RGO) sheets are synthesized and decorated with ruthenium nanoparticles. This Ru-RGO composite has future scope in energy storage applications such as secondary batteries and electrochemical double layer supercapacitors.

## 2. Experimental

Graphite powder (<20 µm), potassium permanganate ($KMnO_4$), concentrated sulphuric acid ($H_2SO_4$), sodium nitrate ($NaNO_3$), hydrogen peroxide ($H_2O_2$), hydrazin hydrate, ammonia solution were used as received.

About 1gm of graphite powder was added to 23 ml of cooled (0˚C) concentrated $H_2SO_4$. About 3gm of $KMnO_4$ was added in the solution gradually with stirring and cooling, after that mixture was stirred at 35˚C for 30 min. The 46 ml of distilled water was slowly added and the mixture was kept at room temperature for 15 min. The reaction was terminated by adding 140 ml of distilled water followed by 10 ml of 30% $H_2O_2$ solution. The solid product was separated by centrifugation and washed repeatedly with 5% HCl solution until sulphate could not be detected with $BaCl_2$. This washed product was kept in air-oven at 65˚C overnight. Thus obtained GO powder is used for further analysis. The ontained GO powder is suspended in 30 ml DI water followed by addition of 40 µl of hydrazine solution and 100 µl of ammonia solution with continuous stirring at 60°C for 30 minutes. This dried black precipitate used as RGO for further characterization[3,4].

10 mg RGO was taken and dispersed in 20 ml of ethylene glycol-water solution in the ratio of (3:2). After complete dispersion, 6.4 mg $RuCl_3$ was added and the mixture was heated at 125 °C for 4 hours. After 4 hours mixture was cooled naturally. The product was separated by centrifugation and washed with ethanol and with distilled water.

The prepared Ru-RGO composite was characterized for structure and morphology analysis using X ray diffraction (XRD) (D8 Advance X-ray diffractometer with Cu $K_{alfa}$ radiation (k = 0.15418 nm, Bruker) and TEM (FEI, Tecnai, $G^2$-U twin operated at 200kV), respectively. Raman spectrum was carried out on a Renishaw Raman spectrometer with a 514 nm laser at a power of 5%.

## 3. Results and discussion

Figure 1 shows XRD patterns of RGO and Ru-RGO, respectively. For RGO, two broad peaks observed at angle $23.68^0$ and $41.19^0$ suggesting the reduction of graphitic carbon and restoration of the carbon $sp^2$ bond with well-ordered 2 dimensional sheets. A broad spectrum at angle 23.68 clearly suggest that this spectrum represents presence of RGO. The red XRD spectrum with single peak represents Ru-RGO diffraction pattern. A broad peak at angle $42.9^0$ observed, which is clearly indicates presence of Ruthenium with plane (104)[5].

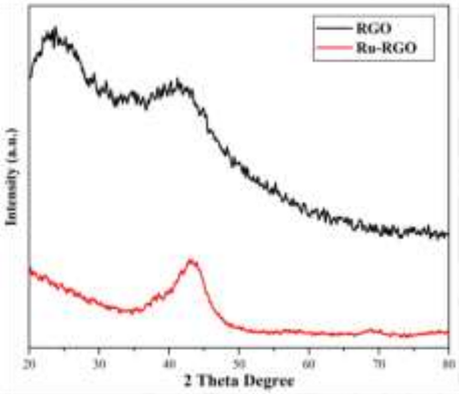

*Figure 1 XRD spectra of RGO & Ru-RGO*

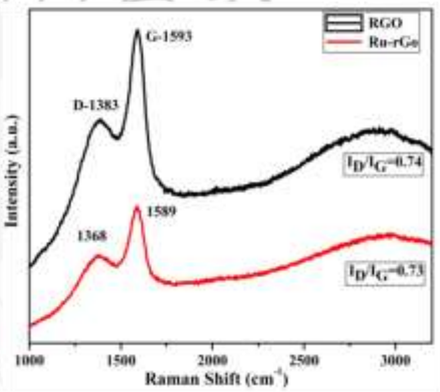

*Figure 2 Raman Spectra of RGO & Ru-RGO*

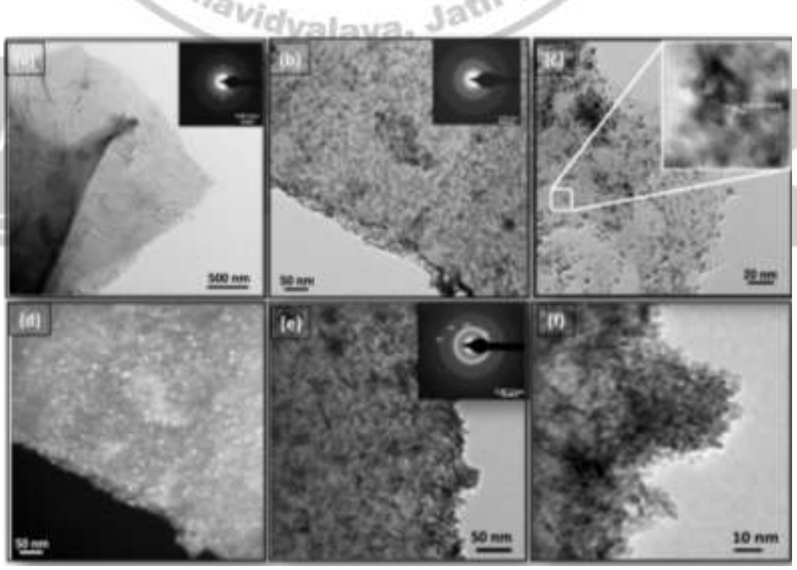

*Figure 3: (a) TEM image of RGO, (b, c, d, e & f) TEM image of Ruthenium decorated RGO (inset a,b and e respective SEAD pattern.*

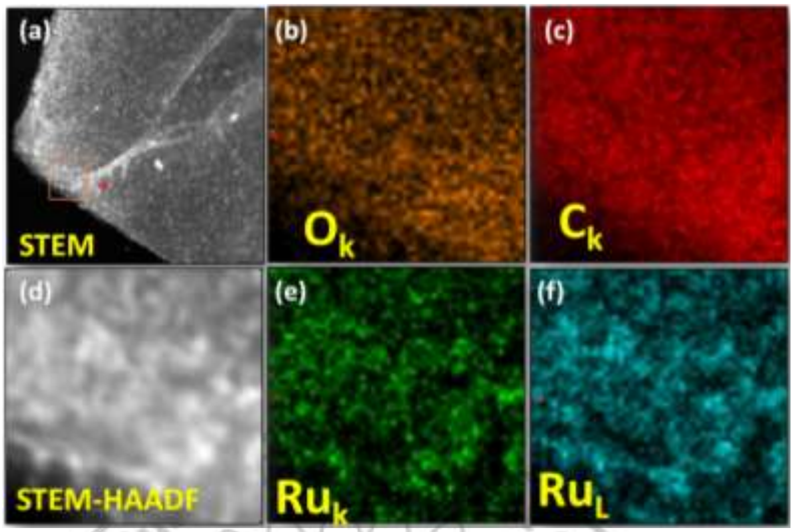

***Figure 4: (a) High angle annular dark field image of RGO (b, c, d, e & f) STEM-EDS elemental mapping of Oxygen, Carbon and Ruthenium***

Figure 2 represents two spectrum of RGO and Ru-RGO respectively. Both the Raman spectra indicates presence of graphitic carbon layers. The peak at 1593 $cm^{-1}$ corresponding to the G-band was up-shifted compared with that of graphite which clearly indicates that formation of reduced graphene oxide. This was attributed to the presence of isolated double bonds that resonate at frequencies higher than that of the G-band of the graphite. The G-band of RGO occurred at 1593 $cm^{-1}$, which corresponds to the recovery of the hexagonal network of carbon atoms with defects. The intensity of the two-dimensional (~2910 $cm^{-1}$) peak is not improved, showing better graphitization or no charge transfer due to the absence of impurities in RGO. In Ru-RGO raman spectra there is change in $I_D/I_G$ ratio with presence of Ruthenium[5,6,7].

Figure 3 represents transmission electron microscopy (TEM) images and selected area electron diffraction (SAED) pattern, respectively. These images indicate that RGO sheets are multilayered. SAED pattern shows diffraction spots arranged in hexagonal manner which states single crystal structure of RGO. Figure 3 b, c, d, e and f shows ruthenium decorated reduced graphene oxide sheets. The HR-TEM demonstrate that the ultrafine ruthenium nanoparticles with size 2 - 6 nm have been decorated on the graphene sheets. Figure 4 shows high angle annular dark field image with Energy dispersive X-ray spectroscopy elemental mapping (HAADF-EDAX mapping) of Ru-RGO. This indicates presence of Ruthenium on RGO sheets[7,8]. The composite comprising uniformly dispersed Ru ultrafine particles on multilayer RGO can be used as electrode material for supercapacitor as well as Li-ion secondary batteries

## 4 Conclusion.

**In conclusion, Hummer's method have been successfully employed to obtain multilayer reduced graphene oxide sheets. In combination with transition metals, this RGO sheets can be useful for various applications like field emission study, hydrogen evolution, drug delivery, sensors, super-capacitors, hydrogen storage, composites, coatings, paint ink, transparent conductive layers, dye-sensitized solar cells and bio-applications.**

## References

1. Castro Neto, et.al. *Reviews of Modern Physics* **2009,** *81*, 109.
2. Moon, I. K et.al. *Nat Commun* **2010,** *1*, 73.
3. Zhang, J et.al. *Chem Commun (Camb)* **2010,** *46*, 1112.
4. Chen, J.; Yao et.al. *Carbon* **2013,** *64*, 225.
5. Marcano, D. C et.al. *ACS Nano* **2010,** *4*, 4806.
6. Cheng, N. et.al. *American Journal of Analytical Chemistry* **2012,** *03*, 312.
7. Uddin, M. E. ET.AL. *Composites Part B: Engineering* **2015,** *80*, 238.
8. Wang, A. *Sci Rep* **2016,** *6*, 23325.
9. Haldorai, Y. ET.AL. *Electrochimica Acta* **2014,** *120*, 65.
10. Zhang, J. ET.AL. *Chem Commun (Camb)* **2010,** *46*, 1112.

# Studies of Yettrium Telluride Electrodeposited Thin Films.

R.D. Mane and P.P. Chikode
Department of Physics,Jaysingpur College, Jaysingpur-416 101.Maharashtra, drmanerd@gmail.com
Corresponding author e-mail-prashantchikode@gmail.com

## Abstract:

**The YTe thin films were prepared on stainless steel substrate and Fluorine doped Tin Oxide (FTO) coated glass plates from an aqueous bath by electrodeposition technique. These films were deposited by varying the deposition time. The thickness of film deposited, mass of YTe deposited onto substrate and the rate of deposition have been measured. Then it is estimated that it is possible to measure the stress developed in these films. These films were characterized by using optical absorption, SEM and X-ray diffraction techniques.**

**KEYWORDS: Electrodeposition, X-ray diffraction, , Microstructure, SEM, Optical absorption.**

## 1. Introduction

Recently rare earth metals and their compounds are attracting a great deal of interest due to their use in high temperature superconductivity and other applications in magnetic, electric and high temperature devices [**1-5**]. These compounds have the simplest NaCl structure. Some work has been reported on electrical, optical and photoelectrical chemical properties of chalcogenides of Samarium and Dysprosium [**6**].

Thin films of chalcogenides of various rare earths have been prepared by multisource evaporator system. A thin film method offers a unique way of examining the basic magnetic interactions and at the same time produce structures with potential applications in areas such as micromotors or magneto-optical recording [**7**]. Rare earth selenides and tellurides have shown semiconducting properties and their potential application in thermoelectric generation. Yttrium Selenide (YSe) thin films on stainless steel substrate were found to be well adherent and uniform. The nature of contact between YSe and stainless steel is ohmic and bandgap is about 1.6 eV. It has been reported on the sequential electrodeposition of $CdSe_{0.65}$ $Te_{0.35}$ on to FTO coated substrates [**8,9**]. Electrodeposition of Y-Ba-Cu from aqueous and non-aqueous baths has been reported by Slezak and Wiekowski [**10**].

## 2. Experimental

Thin film electrodeposition was carried out by using a three electrode system with a saturated calomel electrode (SCE) as the reference electrode. The well cleaned , mirror polished, stainless steel glass plate as a working electrode with graphite as a counter electrode. Applied potentials were measured with respect to SCE. The fluorine doped tin oxide (FTO) substrates were cleaned ultrasonically with 0.1 M NaOH, double distilled water, acetone and finally cleaned in double distilled water.

YTe has been carried out from nonaqueous baths. The preparative parameters such as temperature, pH, concentrations, and potential etc. have been optimized. An YSe and YTe thin films have been electro synthesized on stainless steel and Fluorine doped Tin Oxide (FTO) coated glass substrates. The thin films of chalcogenides of various rare earths such as Sm,Tm,Yb,$Sm_{1-x}Ln_xS$,$SmS_{1-x}$,$AS_x$,$TmTe_{1-x}Se_x$, $Sm_{1-x}Yb_x$ S etc. have been prepared by multisource evaporator system. Their electrical, optical, magnetic structural and other properties have been studied and theoretical models have been proposed [**7**]

## 3. Results And Discussion

### 3.1 X-ray diffraction

Thefilms were characterized with an optical absorption, X-ray diffraction, and micrographs. The structural properties of the films are studied by XRD pattern using X-ray diffractometer (Pilips Pw – 1710) with CuKα radiation. We have prepared the Yttrium chalcogenides thin films on stainless steel substrates. The X-ray diffraction technique can be used to determine the crystalline nature of solids, the nature of the phases present and to calculate structural parameters.

The substance is present in the in the pure state or as one constituent of a mixture of substances, which produces a characteristic diffraction pattern. The qualitative and quantitative analysis is also possible in the diffraction method of chemical analysis The structural identification of YTe thin film was carried out by using X - rays diffraction in the range of diffraction angle 2θ between $10^0$ and $100^0$. It was found from XRD pattern, that the films were cubic structure with preferred orientation along (220) plane. The d-values of XRD reflection were compared with standard d-values taken from Joint Committee on Powder Diffraction on Standards (JCPDS) data are shown in **Table 1.** The XRD pattern of the yttrium telluride thin film from the aqueous bath at room temperature on stainless steel substrate is as shown in **Fig. 1.** The film is polycrystalline with orientation along (2 2 0), (2 2 2), (4 2 2), (4 4 0) planes.

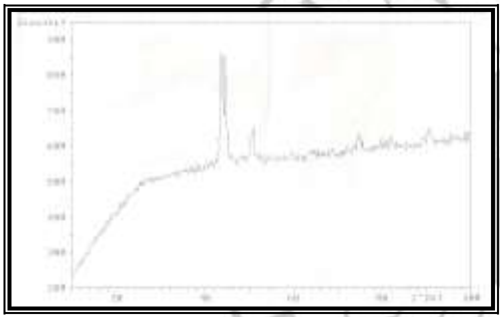

**Fig.1** XRD pattern of deposited YTe thin film.

| Sr.No. | Angle $2\theta^0$ | Observed d values $A^0$ | Standard d values $A^0$ | Plane h k l | Composition | Structure |
|---|---|---|---|---|---|---|
| 1 | 43.720 | 2.0688 | 2.15 | (220) | YTe | Cubic |
| 2 | 50.710 | 1.7988 | 1.751 | (222) | YTe | Cubic |
| 3 | 74.834 | 1.2678 | 1.244 | (422) | YTe | Cubic |
| 4 | 90.580 | 1.0839 | 1.077 | (440) | YTe | Cubic |

**Table:1** The inter planer distance compared with standard d values for YTe thin film.

### 3.2 Optical absorption studies

The optical absorption studies were carried out in the wavelength range 350 to 850nm using UV-VIS-NIR spectrophotometer (Hitachi model 330) to determine the band gap energyEg. The surface morphology of yttrium selenide and yttrium telluride chalcogenide thin films has been studied by optical microphotographs. YSe and YTe chalcogenide thin films show some fine cracks in films.

### 3.3 Microstructural and SEM studies

To study the surface morphology of the materials German make LeitzOrthoplan Optical microscope was used. The transmission mode is used for YTe films on FTO coated glass substrate by using magnification 40X. From the microstructural studies the nature of the deposit and distribution of grains on the film surface as well as the effect of some of the preparative parameters on microstructure are found. Micrograph in Fig.2 and scanning electron micrograph shown in fig 3 reveals that the films are uniform, dense and adherent to the substrate.

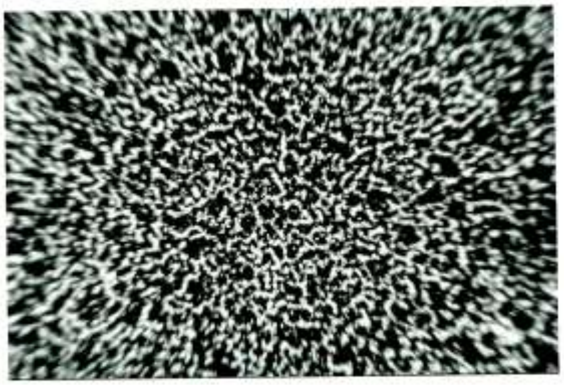

Fig.2: Microphotograph of YTe thin film.

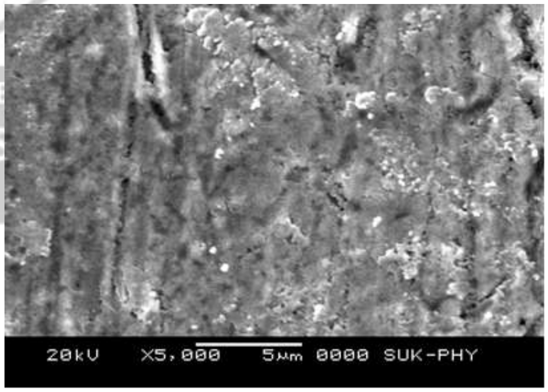

**Fig.3:** SEM image of YTe thin films for magnification X5000.

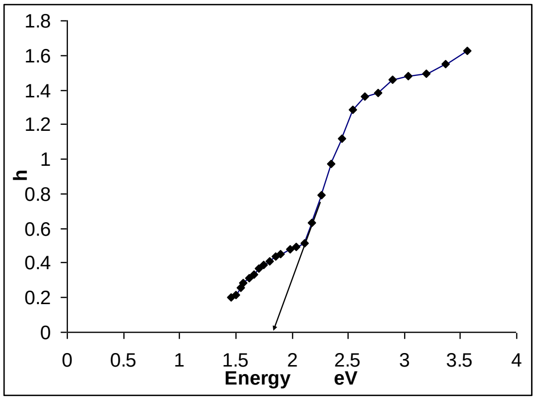

**Fig.4** The variation of $(\alpha h\nu)^2$ versus hν for YTe thin film.

The optical absorption has been carried out in the wavelength range of 350 to 850 nm. YTe thin film is estimated as 0.144μm. The fig. 4 shows the variation of $(\alpha h\nu)^2$ as a function of photon energy hν. Extrapolation of the straight line portion to zero absorption coefficient ($\alpha$=0) leads to the estimation of band gap energy ($E_g$). These films were deposited on to F.T.O. coated glass substrate and absorption was recorded in the wavelength range of 350 nm to 850 nm employing UV-VIS-NIR spectrophotometer.

## 4. CONCLUSIONS:

**Electrodeposition for synthesis of YTe thin film is feasible technique. These thin films are deposited at optimized preparative parameters are dark and grayish in color and well adherent to the substrate. It is possible to determine the thickness and stress developed in these films by using optical techniques such as holographic interferometry. As a continuation of this work we are going to measure the stress and thickness developed in thin films. These YTe thin films can be used in magnetic, optical, nuclear and thermoelectric devices. The rare earth selenides and tellurides have showed semiconductor properties and their potential applications in thermoelectric generation.**

## Acknowledgement

The authors are thankful to U.G.C. , New Delhi for supporting this work under the scheme of minor research project.

## References

1. B.T. Mathias, R.M. Bozorth and J.M. Vahvleck, Phys.Rev.Lett.,7(1961),p. 160.
2. D.S. McClure and Z.J. Kiss, Chem. Phys. 39(1963), p.3251.
3. K. Rajeshwar, J.Appl.Electrochem. 15(1985), p.1.
4. G.J. McCarthy and J.J. Rhyne, The rare earths in modern science and Technology, (Plenum 5. Press New York), (1978).
5. N.Sclar, J.Appl.Phys.35 (1964), p.1534.
6. R.J.Reid, L.K.Matson, J.F.Miller and R.C.Himes, J. Electrochem. Soc.111(1964), p. 943.
7. Suryanarayanan R. and BrunG.,Thin Solid Films,35(1976),p.263.
8. C.D.Lokhande, B. Electrochem, 3(3) (1987), p.219.
9. C.D.Lokhande, B.Electrochem. 7(7) (1991), p.319.
10. P. Slezak and A. Wieckowski, J. Electrochem. Soc. 138 (1991),p. 1038.

# Effect of rotational Wiggling on speckle contrast

P.P. Padghan┼, P. P. Rathi and K.M. Alti*
Department of Physics, Sant Gadge Baba Amravati University, Amravati, Maharashtra, India
*Author for Correspondence E-mail: kamleshalti@sgbau.ac.in
┼Presenting author E-mail: punam.payalrathi@gmail.com

## Abstract

**In this article we have reported the effect of wiggling of rotating object on speckle contrast using Electronic Speckle Pattern Interferometry. The speckle correlation fringes were recorded observing any changes in the surface during rotation. Interesting periodic change in the speckle contrasts were seen due to rotation. After the study of above things, movement at back and forth with quick irregular motions known as wiggling can be observed for rotating body.**

**Keywords**
**Electronic speckle pattern interferometer (ESPI), speckle patterns, speckle contrast, wiggling**

## Introduction

Non-destructive evaluation of an object can be done by optical based methods, such as digital phase shifting methods and electronic speckle pattern interferometer[1], [2]. Electronic speckle pattern interferometer (ESPI) was developed in 1970s by J. N. Butters and J. A. Leendertz [3]. In this method object beam is interfere with reference beam and form speckle pattern. Using this method various deformations on object can be measured such as mechanical deformation [4], thermal deformation[5], acoustical deformation etc. In addition to this ESPI is largely used in metrology as well as in medicine [6]–[9]. Deformation in object can be studied by correlating initial and final shape of an object [10]. If the shape of object is changed, fringes are obtained which are corresponding to changes in the degree of correlation of the two speckle patterns. These fringes are called as speckle correlation fringes and they form a contour map of surface displacements and give the information about asymmetry. Quality of speckle pattern is generally measured in terms of speckle contrast which is defined as following [11],

$$C = \frac{\sqrt{\langle I^2 \rangle - \langle I \rangle^2}}{\langle I \rangle} \qquad (1)$$

Where, $I$ is the intensity of speckles in speckle patterns, C is the speckle contrast, numerator is the root mean square deviation of the intensity fluctuations and the denominator is average intensity. Value of C lies between 0 and 1, where 0 means no speckle and 1 means image full of speckles. In the present paper we have reported the interesting periodic change in rotating body on the basis of speckle contrast.

## Experimental setup

The Schematic diagram of the experimental setup of electronic speckle pattern Interferometry to study rotating object is as shown in the Fig. 2. In ESPI interferometer technique a laser light of 632.8 A0i.e. 632.8 nm of He-Ne laser with 5 mW output power is used as the light source. Beam splitter splits laser beam in to object beam and reference beam. Object beam illuminates a middle part of object. It means that the effect of a hole made at the edge of object cannot be studied.

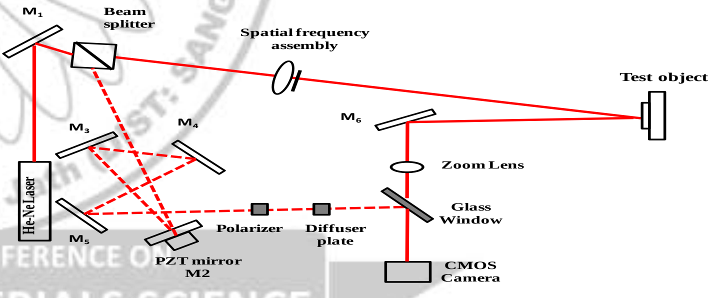

**Fig. 2:** **Schematic diagram of ESPI to study rotating object.**

The information of surface of object is gain by speckle pattern. Another beam known as reference beam from the same source is incident by beam splitter on the CMOS camera. The object beam and reference beams are superimposed and forms a speckle pattern of the object. The speckle pattern is collected by zoom lens and will be show on the CMOS camera. The object is rotated using motor. Motor is connected to power supply. This measurement is perpendicular to object surface so known as out of plane set up. This ESPI setup is use to study the rotating body. The original photograph of ESPI to study rotating object is as shown in Fig.3.

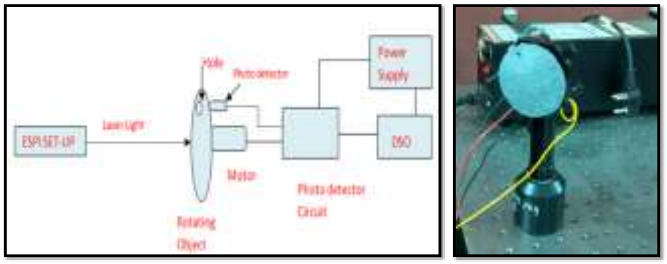

a) b)

**Fig.2: a) Schematic diagram for measuring rotational period of the object using laser; b) Rotating object**

## Result and discussion

The rotating object has 3.5 cm radius and illuminated by laser source. The object beam illuminates the object in middle and not to a whole object. So the wiggling due to a hole at the edge of object is neglected. The reference beam and object beam are superimposed to form speckle pattern. This speckle pattern is collected with the help of CMOS camera. The video of 60 sec is taken. This video is converted to frames using *VirtualDub-1.10.4* software. Thus there are total 530 frames. The time required for completing one cycle is found to be 0.9 sec which is calculated with the help of DSO. Thus in 0.9 sec there is total 8 frames. So in one complete rotation of rotating body i.e. for one cycle there are total 8 frames. Eight speckle patterns were recorded and compared to each other. After comparing if the results are null then it implies to no wiggle. In case of wiggle in rotation the subsequent images upon subtraction shows non-zero values. The difference of subsequent frames can be taken out for one cycle. The recorded experimental correlation fringes using electronic speckle pattern interferometry are as shown in the Fig 3. The black images show the zero difference. It means there is no wiggle. If the difference is non zero then there is a wiggle in rotation.

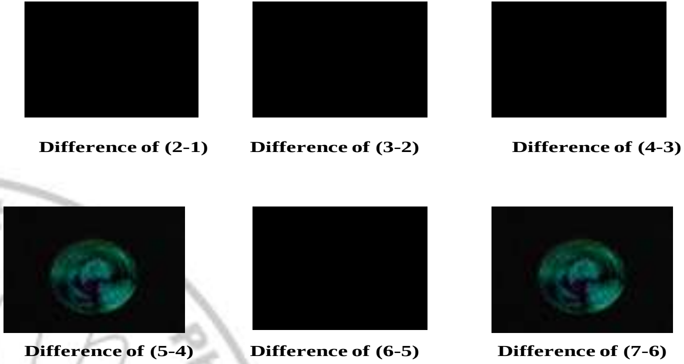

**Fig.3: Experimental correlation fringes for a first cycle.**

The graph of the time (in sec) and contrast of images is shown in Fig. 4. By observing the graph it has seen that there is a periodic change in the speckle contrast. Amplitude is not same for all images. It is less for some images and high for some images.

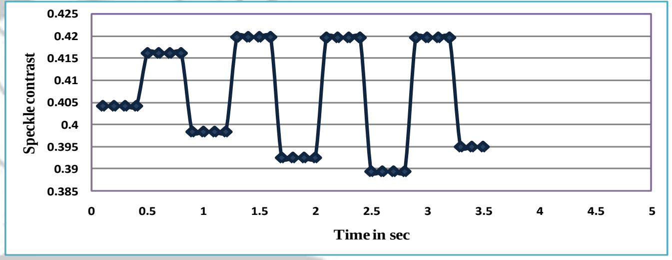

**Fig. 4: Variation of speckle contrast with rotation**

## Conclusion

**We have reported the wiggling in rotating object using electronic speckle pattern interferometry. Speckle correlation fringes were recorded of a rotating object. In each complete rotation, eight speckle patterns were recorded and compared to each other. After correlating these speckle patterns the correlation fringes shows null which implies there is no wiggle. If correlation fringes shows valid pattern then it implies there is wiggling in the object. While studying this interesting periodic variation of speckle contrast was observed due to wiggling in rotating object.**

## References

[1] L. X. Yang, et al *Measurement*, vol. 16, no. 3, pp. 149–160

[2] “Phase-measurement interferometry techniques for nondestructive testing.pdf.” .

[3] J. N. Butters and J. a Leendertz, *J. Phys. E.*, vol. 4, no. 4, pp. 277–279, 1971.

[4] I. M. De la Torre, et al *Opt. Lasers Eng.*, pp. 1–27, 2016.

[5] C. Casavola, et al, *Strain*, vol. 49, no. 6, pp. 497–506, 2013.

[6] Y. Beiderman, et al *J. Biomed. Opt.*, vol. 15, no. 6, p. 061707, 2

[7] B. Kemper, D. Dirksen, W. Avenhaus, a Merker, and G. von Bally, *Appl. Opt.*, vol. 39, no. 22, pp. 3899–3905, 2000.

[8] J. Soons, P. Lava, D. Debruyne, and J. Dirckx, *J. Mech. Behav. Biomed. Mater.*, vol. 14, pp. 186–191, 2012.

[9] W. Avenhaus, et al *Gastrointest. Endosc.*, vol. 54, no. 4, pp. 496–500, 2001.

[10] P. P. Padghan and K. M. Alti, *RRJoPHY Res. Rev. J. Phys.*, vol. 4, no. 2, pp. 1–7, 2015.

[11] S. Roelandt, et al Janssens, and H. Thienpont, vol. 20, no. 8, pp. 131–137, 2012.

# Bryophytes as Source of Silver Nanoparticles: A Review

Lavate, R.A., Sathe, S.S., *Kumbhar, D.A., *Salunke, G.D. *Mali V.C., *Bobade, N.R. and M.B. Sajjan**
Department of Botany, Chemistry* and Zoology **
Raje Ramrao College, Jath, Maharashtra, India.

## Abstract

**Bryophytes are primitive land plants showing simple organization of the thalloid plant body. In terms of species richness, bryophytes are the second largest group of plants having *ca.* 28,000 species worldwide of which around *ca.* 2489 species are distributed in different phytogeographical regions of India mainly diversified in Himalayas, Western Ghats and Eastern Ghats. The phytochemical work on these primitive plants shows that they possess a variety of chemicals and therefore can be used in many ways. As compared to angiospermic plants, bryophytes are advantageous as the interference of the biochemicals could be lower due to their simple primitive organization of body. The present review briefly focuses on the simple eco-friendly, one step process of biosynthesis and methods used in characterizing of silver nanoparticles from bryophytes and their application.**

## Introduction

Biosynthesis is a novel way to synthesize nanoparticles by using biological sources. It is gaining much attention due to its cost effective, eco friendly and large scale production possibilities. Nanomaterials are the atomic and molecular building blocks (~0.2 nm) of matter. Nanoparticles belong to a wider group of nanomaterials having amorphous or crystalline form and their surfaces can act as carriers for liquid droplets or gases (Buzea et al 2007). Nanoparticles have been in use in pottery and medicine since ancient times. Since last decade the most effectively studied nanoparticles are those made from the noble metals such as silver, gold and platinum (Duran *et al*., 2005; Ankamwar, 2010; Deng *et al*., 2009).

Traditionally, silver metal is used to control bodily infection and prevent food spoilage. Silver is used as wound healer agents and ulcer treatment due to excellent physico-chemical properties, nanoparticles have potential applications in all fields of science and technology. Since ancient times human society use medicines, from gold, silver, mercury, sulphur, mica, arsenic, zinc, other minerals, gems, shells, horns treated with indigenous herbs as bhasmas (a fine ash obtained through Incineration) and chendurams (prepared by the process of sublimation and they are much more potent than bhasmas). Nanoparticle has multifunctional properties and very interesting applications in various fields such as medicine, nutrition and energy (Chandran *et al.*, 2006).

Biosynthesis of nanoparticles using plant extracts is the latest most favorite method of green, eco-friendly production of nanoparticles as it offers one step. Currently it is exploited to a vast extent because the plants are widely distributed, easily available, safe to handle and with a range of metabolites (Kulkarni *et al.*, 2012 a, b). Biosynthesis methods have more compensation over other classical synthesis procedures due to the availability of more biological entities and eco-friendly procedures. The rich biodiversity and easy availability of plant entities have been highly explored for the nanomaterials synthesis (Monda *et al*., 2011). Silver is the one of the most commercialised nano-material with five hundred tons of silver nanoparticles production per year (Larue et al., 2014) and is estimated to increase in forthcoming years. Silver nanoparticles have also gained significance due to their broad-spectrum activity against bacterial infections. Plant crude extract contains novel secondary metabolites such as phenolic acid, flavonoids, alkaloids and terpenoids in which these compounds are mainly responsible for the reduction of ionic into bulk metallic nanoparticles formation (Aromal and Philip, 2012). These primary and secondary metabolites are constantly involved in the redox reaction to synthesize eco-friendly nanosized particles. Many previous reports are demonstrating that biosynthesized nanoparticle effectively controlled oxidative stress, genotoxicity and apoptosis related changes (Kim et al., 2007).

Bryophytes are primitive land plants showing simple organization of the thalloid plant body (Crandall-Stotler, 1980).The bryophytes possess a variety of chemicals and therefore can be used in many ways. (Asakawa, 2007; Duran, 2005; Kulkarni, 2011, 2012a&b; Srivastava *et al*., 2011). As compared to Angiospermic plants, Bryophytes are advantageous as the interference of the biochemicals could be lower due to their simple primitive organization of body. The work on bryophytes regarding biosynthesis of nanoparticles is quite meager as compared to other plant groups. Kulkarni *et al.* (2011, 2012a, b) and Srivastava *et al.* (2011), have investigated *Riccia* sps., *Anthoceros* sps. and *Fissidens minutes* for the synthesis of silver nanoparticles and their antibacterial activity. Keeping in mind the above fact the present review has been undertaken.

**Methods used to synthesize nanoparticles**

Traditionally nanoparticles were produced only by physical and chemical methods. Some of the commonly used physical and chemical methods are Ion sputtering, Solvothermal synthesis, Chemical reduction, Laser ablation, Inert gas condensation and Biosynthesis of nanoparticles. and Sol gel technique *etc.* (Bindhu & Umadevi, 2015; Mahdi *et al.*, 2015; Padalia *et al*., 2014; Sre *et al.*, 2015). Basically there are two approaches for nanoparticle synthesis (Fig. 1 and 2) *viz.*, the Bottom up approach and the Top down approach (Iravani *et al.*, 2013).

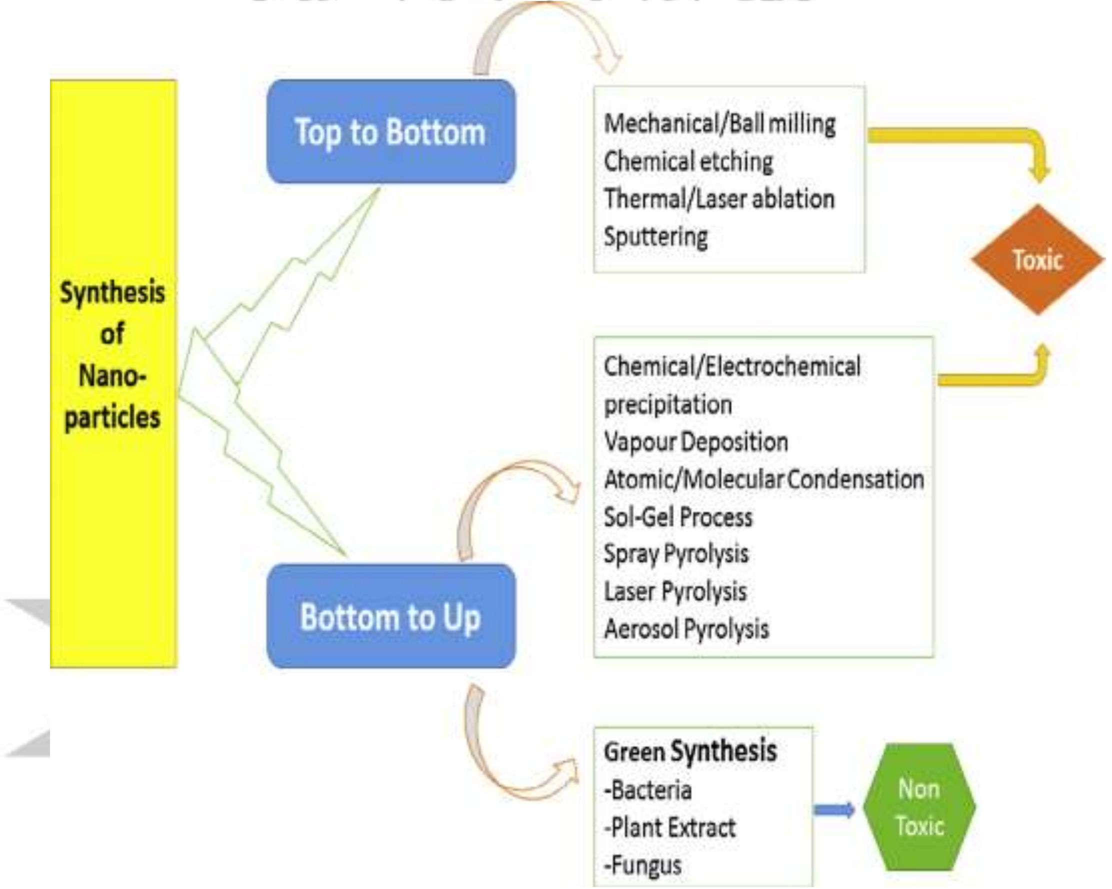

**Fig. 1:** Different approaches of synthesis of silver nanoparticles. (Source: Ahmed *et al.*, 2016)

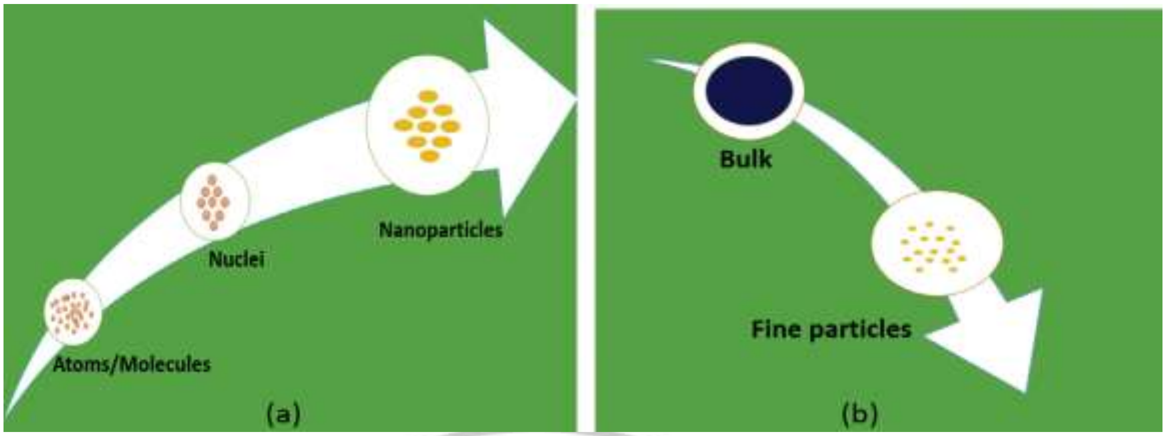

**Fig. 2:** Protocols employed for synthesis of nanoparticles (a) bottom to top approach and (b) top to bottom approach (Source: Ahmed *et al.*, 2016)

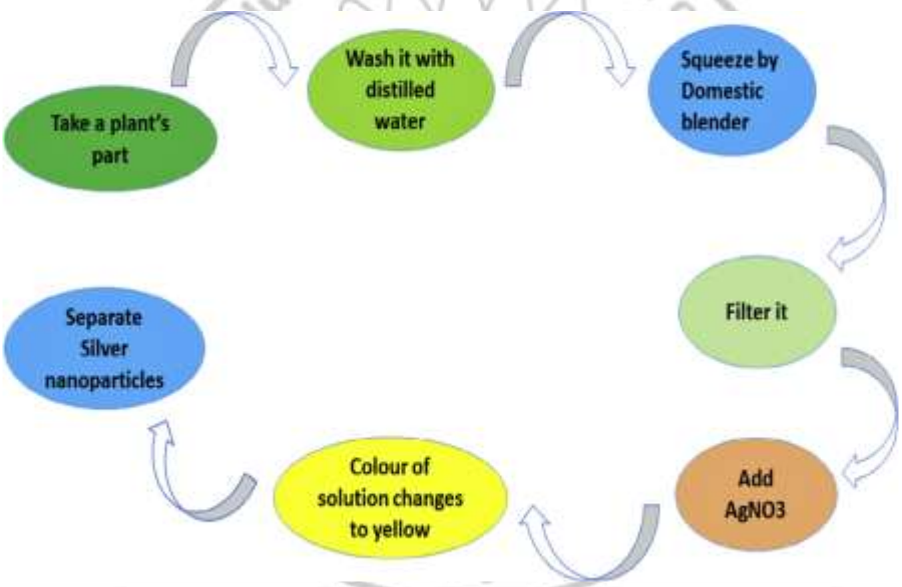

**Fig. 3:** Protocol for synthesis of silver nanoparticles using plant extract. (Source: Ahmed *et al.*, 2016)

## Green syntheses of silver nanoparticles using Bryophytes

Green syntheses of AgNPs have been performed using plant extracts, microbial cell biomass or cell free growth medium and biopolymers. The plants used for AgNps synthesis range from algae to angiosperms; however, limited reports are available for lower plants and the most suitable choice are the angiosperm plants. The bryophytes possess a variety of chemicals and therefore can be used in many ways. (Asakawa, 2007; Duran, 2005; Kulkarni, 2011, 2012a, b; Srivastava, 2011). As compared to Angiospermic plants, Bryophytes are advantageous as the interference of the biochemicals could be lower due to their simple primitive organization of body. The work related AgNPs synthesis using Bryophytes is summarized in table 1.

**Table1: Summary of the work related AgNPs synthesis using Bryophytes.**

| Sr. No. | Extraction Method | Operating Conditions | Method of Characterization | Particle Characteristics | Pharmacoloical Applications | References |
|---|---|---|---|---|---|---|
| 1 | Ethanol filtrate of *Riccia* | 1 mM, 25˚C, dark,<br>5 ml/1 ml,<br>Agitated | UV-Vis<br>SEM<br>EDS | Shape:cuboidal/triangular | Antibacterial activity after incorporation into gauze cloth | Kulkarni *et al.*, 2012a |
| 2 | Ethanol filtrate of *Anthoceros* | 0.5 mM, 10 min, room temp.<br>5ml/1 ml, Static | UV-Vis<br>SEM<br>EDS | Size:20 - 50 nm<br>Shape: cuboidal/triangular | Antibacterial activity *against Pseudomonas aeruginosa* | Kulkarni *et al.*, 2012b |
| 3 | Aqueous and ethanol filtrate of *Fissidens minutes* | 0.5 mM, 1 hr, room temp.<br>10 ml/1 ml, Shaken | UV-Vis<br>SEM<br>EDS | Shape:nearly spherical | Antibacterial action against *E.coli*, *B. cereus*, *K.pneumoniae*,<br>*P. aeruginosa* | Srivastava *et al.*,<br>2011 |
| 4 | Aqueous filtrate of *Anthoceros* | 1 mM, 25˚C, dark,<br>5 ml/1 ml,<br>Agitated | UV-Vis<br>SEM<br>EDS | Size:20 - 50 nm<br>Shape: cuboidal/triangular | Antibacterial action against *E. coli*, *B. subtilis*, *K. pneumoniae*,<br>*P. aeruginosa* | Kulkarni *et al.*, 2011 |

**Characterization of silver nanoparticles:**

The characterization study of silver nanoparticle was done by the examining size, shape and quantity of particles. Number of technique is used for this purpose, including UV-visible spectroscopy, Scanning Electron Microscopy (SEM), Fourior Transmission Infrared Spectroscopy (FTIR), X-Ray Diffraction (XRD), and Dynamic Light Scattering (DLS) ( Wang, et al., 2000).

Fig. 1. UV-Vis spectrum of silver nanoparticles

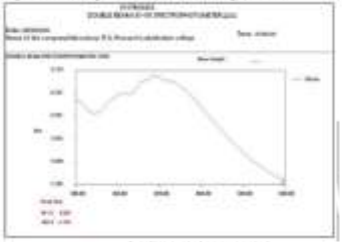

Fig. 2. Change in colour of the extract after synthesis of nanoparticles

Fig.4 SEM image of the silver nanoparticles

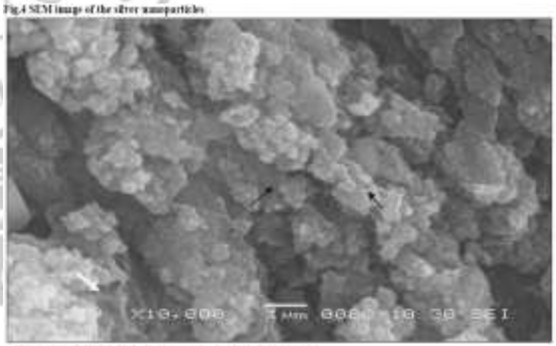

Fig. 3. EDS spectrum of silver nanoparticles

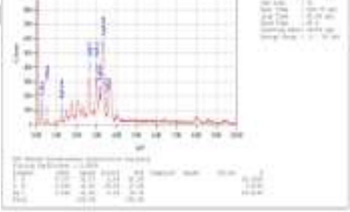

Fig. 5 SEM of the gauze cloth disc

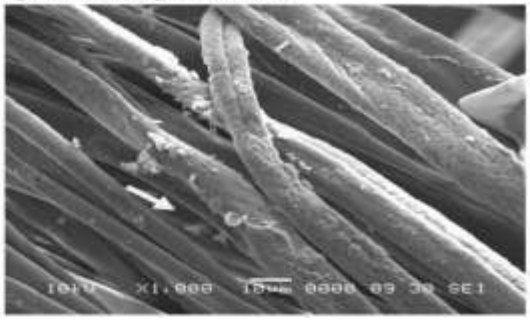

**Fig. 4:** Silver nanoparticles of *Anthoceros* and its characterization by various techniques.(Source: Kulkarni et al., 2012 a).

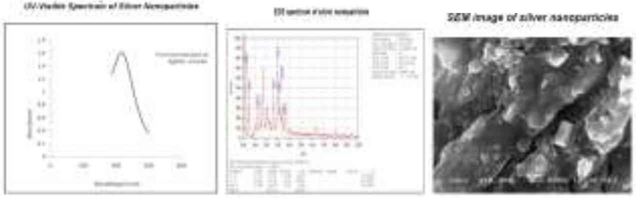

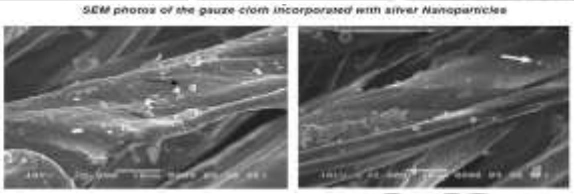

**Fig. 5**: Silver nanoparticles of *Riccia* and its characterization by various techniques. (Source: Kulkarni et al., 2012 b).

**Antibacterial of Silver Nanoparticles (Fig : 6, 7 and 8)**

It is well known that silver ions and nanoparticles are highly toxic to microorganisms. Silver nanoparticles have been known to have inhibitory and bactericidal effects and thus we extend its application as an antibacterial agent. The Antibacterial activity is estimated by the zone of inhibition (Srivastava, 2011).

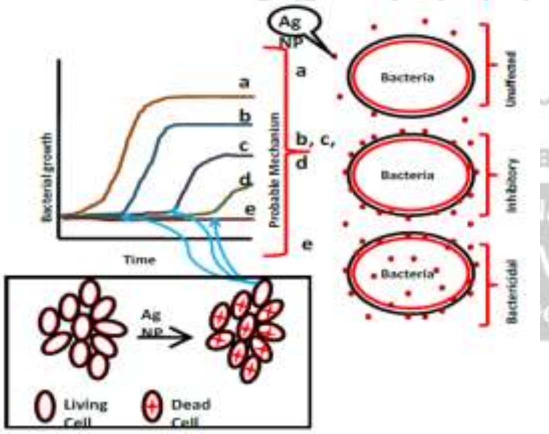

**Fig 6.** Mechanism of antibacterial action of AgNPs. (Source: Srikar *et al.*, 2016).

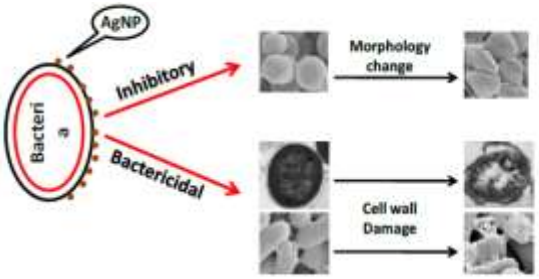

**Fig. 7**: Morphological change and cell wall damage of bacterial cell. (Source: Srikar *et al.*, 2016).

**Fig. 8:** Antibacterial activity of gauze cloth discs against *Pseudomonas aeruginosa* (Kulkarni et al., 2012)

## Conclusion

**Plants are the important sources for the living organisms including human beings. The work on bryophytes regarding biosynthesis of nanoparticles is quite meager as compared to other plant groups. Bryophytes prove to be a novel source for biosynthesis of silver nanoparticles. Due to their simple organization of thallus, the extraction and synthesis of nanoparticles is a facile process. The gauze incorporated nanoparticles show antibacterial activity and therefore can be used on a large scale to avoid bacterial infections especially in case of burns and skin problems. The silver nanoparticles synthesized from bryophytes seem to be promising and effective antibacterial agent. Kulkarni *et al.*, (2011, 2012a, b) and Srivastava *et al.*, (2011) have investigated *Riccia* sps., *Anthoceros* sps. and *Fissidens minutes* for the synthesis of silver nanoparticles and their antibacterial activity. The present review will be helpful to give new vistas to amateur scholars about future scope and to do further investigations about use of the bryophytes in the biosynthesis of silver nanoparticles and their antimicrobial property.**

## ACKNOWLEDGEMENTS

Authors are grateful to Principal Dr. S.Y. Hongekar, Raje Ramrao College, Jath for providing necessary encouragement and facilities.

## REFERENCES

**Ahmed, S., Ahmad, M., Swami B. L., Ikram, S. (2016).** A review on plants extract mediated synthesis of silver nanoparticles for antimicrobial applications: A green expertise. *Jour. of Adv. Res.* **7:**17-28.

**Ankamwar, B. (2010).** Biosynthesis of Gold Nanoparticles (Green-Gold) Using Leaf Extract of *Terminalia catappa*. *E-Jour. of Chem.*, **7(4):**1334-1339.

**Aromal, S.A., Philip, D., (2012).** Green synthesis of gold nanoparticles using *Trigonella foenum-graecum* and its size dependent catalytic activity. *Spectrochim. Acta* A **97:**1-5.

**Asakawa, Y., (2007).** Biologically active compounds from bryophytes, *Pure Appl. Chem*., **79 (4):** 557-580.

**Bindhu, M. R., and Umadevi, M. (2015).** Antibacterial and catalytic activities of green synthesized silver nanoparticles. *Spectrochimica Acta* Part A: Molecular and Biomolecular Spectroscopy, **135:**373-378.

**Buzea, C., Pacheco, II, Robbie, K. 2007.** Nanomateriales and nanoparticles: Sources and toxicity. Biointerphses, **2(4):** 17-71.

**Chandran, S.P., Chaudhary, M., Pasricha, R., Ahmad, A., Sastry, M., (2006).** Synthesis of gold nanotriangles and silver nanoparticles using Aloe vera plant extract. *Biotechnol. Prog.* **22:**577–583.

**Crandall-Stotler, Barbara, (1980).** Morphogenetic designs and a theory of bryophyte origins and divergence. *Bioscience* **30:** 580-585.

**Dandotiya, D., Govindpyari, H., Suman, S. and Uniyal, P.L. (2011).** Checklist of the bryophytes of India. *Arch. Bryol.*. **88:** 1-126.

**Deng, Q.Y., Yang, B., Wang, J.F., Whiteley, C.G., W X.N. (2009).** Biological synthesis of platinum nanoparticles with apoferritin. *Biotechnol Lett.* **10:**1505-9.

**Duran, N., Marcato, P.D., Alves O.L, De Souza, G.I. Posito, E., (2005).** Mechanistic aspects of biosynthesi silver nanoparticles by several *Fusarium oxysporum* tr *Jour. of Nanobiotech.* **3:**8.

**Iravani, S. and Zolfaghari, B. (2013).** Green synthesis of silver nanoparticles using *Pinus eldarica* bark extract. Hindawi Publishing Corporation, *Biomed. Res. Int.*, doi: http://dx.doi.org/10.1155/2013/639725

**Kim, J.S., Kuk, E., Yu, K.N., Jong-Ho, K., Park, S.J., Lee, H.J., Kim, S.H., (2007).** Antimicrobial effects of silver nanoparticles. *Nanomed.*, **3:**95-101.

**Kulkarni, A.P., Srivastava, A.A., Harpale, P.M. and Zunjarrao, R.S. (2011).** Plant Mediated Synthesis of Silver Nanoparticles-Tapping the Unexploited Resources. *Jour. of Nat.Pro. and Pl. Res.*, **1:** 100-107.

**Kulkarni, A.P., Srivastava, A.A., Nagalgaon, R.K. and Zunjarrao, R.S. (2012a).** Phytofabrication of silver nanoparticles from a novel plant source and its application. *Int. J. Pharm. Bio. Sci.*, **3(3):**417-421.

**Kulkarni, A.P., Srivastava, A.A. and Zunjarrao, R.S. (2012b).** Plant mediated synthesis of silver nanoparticles and their applications. *Int. J. Pharm. Bio. Sci.*, **3(4) (b):**121-127.

**Larue, C., Castillo-Michel, H., Sobanska, S., C_ecillon, L., Bureau, S., Barth_es, V. (2014).** Foliar exposure of the crop *Lactuca sativa* to silver nanoparticles: evidence for internalization and changes in Ag speciation. Jour. of Hazard. Mater., **264:**98-106.

**Mahdi, S., Taghdiri, M., Makari, V. and Rahimi-Nasrabadi, M. (2015).** Procedure optimization for green synthesis of silver nanoparticles by aqueous extract of *Eucalyptus oleosa*. *Spectrochimica Acta* Part A: Molecular and Biomolecular Spectroscopy, **136:**1249-1254.

**Monda, S., Roy, N., Laskar, R.A., Sk, I., Basu, S., Mandal, D., Begum, N.A., (2011).** Biogenic synthesis of Ag, Au and bimetallic Au/Ag alloy nanoparticles using aqueous extract of mahogany (Swietenia mahogani JACQ.) leaves. *Colloid Surf.* B **82:** 497–504.

**Padalia, H., Moteriya, P., & Chanda, S. (2014).** Green synthesis of silver nanoparticles from marigold flower and its synergistic antimicrobial potential. *Arab. Jour. of Chem.* http:// dx.doi.org/10.1016/j.arabjc.2014.11.015.

**Sabovljevic, M.** (2004). Comparison of the Bryophyte flora of the three Southern European Main land's: The Iberian, the Apenssine and the Balkan Peninsulas. *Bra.-Blan.* 34: 21-27.

**Shaw, A.J. and Renzaglia, K.S. 2004.** Phylogeny and diversification of bryophytes. *American J. Bot.* **91:** 1557-1581.

**Sondi I. and Salopek-Sondi B. 2004.** Silver nanoparticles as antimicrobial agent: a case study on *E. coli* as a model for Gram-negative bacteria. *J. Colloids Inter. Sci.* **275:** 177–182.

**Sre, P. R. R., Reka, M., Poovazhagi, R., Kumar, M. A. and Murugesan, K. (2015).**Antibacterial and cytotoxic effect of biologically synthesized silver nanoparticles using aqueous root extract of Erythrina indica lam. Spectrochimica Acta Part A: *Mole. and Bio. Spectro.*, **135:** 1137-1144.

**Srikar, S.K., Giri, D.D., Pal, D.B., Mishra, P.K. and Upadhyay, S.N. (2016)**. Green Synthesis of Silver Nanoparticles: A Review. Green and Sustainable Chemistry, 6, 34-56. http://dx.doi.org/10.4236/gsc.2016.61004

**Srivastava, A.A., Kulkarni, A.P., Harpale, P.M. and Zunjarrao, R.S. (2011).** Plant Mediated Synthesis of Silver Nanoparticles Using a Bryophyte: *Fissidens minutes* and Its Anti- Microbial Activity. Int. Jour. of Engin. Sci. and Tech., **3:**8342-8347.

**Wang, Z.L., (2000).** "Transmission electron microscopy and spectroscopy of nanoparticles," in *Characterization of Nanophase Materials*, (Wang, Z. L. Ed.), chapter 3, pp. 37–80, Wiley-VCH, Weinheim, Germany,

# Thank you !


Post-Graduate Department of Physics
ICAMS
2016
Raje Ramrao Mahavidyalaya, Jath (DIST: SANGLI)
INTERNATIONAL CONFERENCE ON
ADVANCES IN MATERIALS SCIENCE
7 – 8 December 2016